Homogenization of size-dependent multiphysics behavior of nanostructured piezoelectric composites with energetic surfaces

Qiang Chen, George Chatzigeorgiou, Fodil Meraghni, Ali Javili

Homogenization of Size-dependent Multiphysics Behavior of Nanostructured Piezoelectric Composites with Energetic Surfaces

Qiang Chen[1], George Chatzigeorgiou[1*], Fodil Meraghni[1], Ali Javili[2]

[1] Arts et Métiers Institute of Technology, CNRS, Université de Lorraine, LEM3-UMR7239, F-57000 Metz, France

[2] Department of Mechanical Engineering, Bilkent University, 06800 Ankara, Turkey

*Corresponding author: georges.chatzigeorgiou@ensam.eu

Abstract

Surface piezoelectricity considering the extended Gurtin--Murdoch coherent interface model has been incorporated into the composite cylinder assemblage (CCA), generalized self-consistent method (GSCM), as well as the multiphysics finite-element micromechanics (MFEM), for simulating the size-dependent multiphysics response of nanoporous materials wherein interface stress and electric displacement prevail. In the case of the CCA/GSCM model, the coherent interface model is implemented through the generalized Young--Laplace equations that govern the variation of the surface stress and the surface electric displacement. Three loading modes are utilized to identify the closed-form solutions for a complete set of Hill's moduli, and piezoelectric and dielectric constants. In the case of the MFEM, surface piezoelectricity is incorporated directly through additional surface energies associated with the elements that stretch along the interface. In order to assess the accuracy of the developed computational approaches, the generalized Kirsch problem under far-field transverse electric displacement loading is developed for recovering electric displacement concentration in the vicinity of the pore boundary. Homogenized properties are generated and critically examined for a broad variety of parameters and dimensions, predicted by the CCA/GSCM and MFEM methods. It is shown that all the predicted effective properties of these two families of homogenization techniques are similar except for the transverse shear moduli

where they show marked differences that are reminiscent of what has been observed in the absence of surface electricity.

Keywords: Nanoporous Materials; Multiphysics Effect; Surface Piezoelectricity; Finite-element Method; Composite Cylinder Assemblage Model; Gurtin--Murdoch Interface

1. Introduction

The advances in science and fabrication technology in the past two decades have enabled the fabrication of materials with microstructures characterized by inclusions or porosities in nanometer ranges (Jelinska et al., 2015; Malgras et al., 2016; On et al., 2021; Yang et al., 2020; Yang et al., 2012). However, much work remains to be done in order to gain a deeper insight into the microstructure-property relationship in this class of materials. It is well-known that the interface/surface between various constituent phases of a nano-sized heterogeneous microstructure can play a crucial role in affecting not only the overall response but also the local stress concentration that may lead to failure due to the significant surface tension/stress (Winter et al., 2017). Moreover, the impact of interfaces at the microscale on the overall and local response increases with the decreasing characteristic size of the embedding inhomogeneities due to the larger surface-to-area ratio and surface energies (Duan et al., 2006).

Quantitative characterization of the interface behavior of nanostructured materials often requires extensive molecular dynamics (MD) simulations or experiments, which have justified that the interface-energy-induced size effects are physically meaningful (Chen et al., 2019; Davydov et al., 2013; Fan et al., 2018; Nguyen et al., 2013). However, the MD simulations and actual experimental tests can be extremely computationally costly or tedious, hence preventing them from being efficiently employed in the parametric studies that aim to understand the microstructure-property relationship over a broad variety of parameters and dimensions. Therefore, interest in

continuum mechanics approaches has attracted extensive attention in light of the potential advantages offered by them.

From a continuum mechanics point of view, interfaces in mechanical problems can be categorized into four types according to their kinematic or kinetic characteristics (Chatzigeorgiou et al., 2017; Firooz et al., 2019; Firooz and Javili, 2019; Javili et al., 2017). In heterogeneous materials, the perfect interface model indicates that the inclusion and surrounding matrix are perfectly-bonded, wherein neither displacement discontinuity nor traction discontinuity is admissible across the interface separating different phases. Clearly, the assumption of the perfect interface in heterogeneous materials is inadequate to describe the physical nature and mechanical behavior of the interface region. Hence, in many cases, an imperfect interface model should be considered to accurately capture the overall composite response and the underlying deformation mechanisms. The elastic interface model is kinematically coherent but kinetically non-coherent. The interface elasticity theory proposed by Gurtin and Murdoch (1975, 1978) has spurred extensive investigations of mechanical problems accounting for surface/interface elasticity and tension (Chatzigeorgiou et al., 2015b; Chen et al., 2018b; Dai et al., 2019; Duan and Karihaloo, 2007; Duan et al., 2006; Jiang et al., 2022; Mogilevskaya et al., 2010). In this model, the interface is viewed as a zero-thickness surface that can be treated as a two-dimensional manifold. The variation of surface stress is related to the traction jump condition formulated into the Young--Laplace equations (Chen et al., 2006) whereas the displacement continuity condition holds at the interface. In contrast to the elastic interface model, in the cohesive interface model, the traction is continuous across the interface while the displacement continuity condition is released. The cohesive interface model originally proposed by Barenblatt (1959; 1962) and Dugdale (1960) is generally accepted, which has been further extended by Needleman and coworkers (Needleman,

1987; Xu and Needleman, 1994). The latter works have been extensively adopted in the literature to track interface separation in heterogeneous materials (Bormann et al., 2019; Elices et al., 2002; Tu and Chen, 2020a, b; Tu and Pindera, 2014; van den Bosch et al., 2007). The general interface model unifies all the aforementioned interface models, allowing for both traction and displacement discontinuities across the interface. The general interface model proposed by Hashin (2002) has been further studied in (Benveniste, 2006; Benveniste and Miloh, 2001; Chatzigeorgiou et al., 2017). The general interface model reduces to both the cohesive and elastic interface models in the limit. For further details, discussions and extensions see (Firooz et al., 2021).

In addition to the mechanical behavior, the piezoelectric response is also of theoretical and technological importance in piezoelectric nanostructures because of their promising applications in microactuators and nanogenerators (Chebanenko et al., 2020; Craighead, 2000; Thabet and Fouad, 2021; Yang et al., 2019; Yu et al., 2022). Recent works have shown that the overall response of dielectric elastomer with interfacial phenomena can be radically different from that of its constituents (Ghosh and Lopez-Pamies, 2022; Lefèvre and Lopez-Pamies, 2017). Despite many efforts that have been devoted to the study of the macroscopic properties of nanosized metal-matrix porous composites with surface elasticity, much fewer studies are found in the literature aimed at investigating the properties of nanoscale piezoelectric materials with surface piezoelectricity (Chen, 2008; Gu and Qin, 2014; Xiao et al., 2011). The molecular dynamics simulations conducted by Zhang et al. (2009) and Dai et al. (2011) provide direct evidence that the piezoelectric coefficients of piezoelectric nanostructures are also size-dependent. Hoang et al. (2013) have further confirmed the existence of surface piezoelectricity effects in piezoelectric nanowires using the first-principle analysis. The finite-element package ANSYS has also been employed to investigate the piezocomposites with incomplete interface conditions by Nasedkin (2021), that is,

only the surface stress effect has been taken into account while the surface electric displacement is neglected.

This contribution deals with the homogenized behavior of the piezoelectric nanoporous materials enhanced with the kinematically coherent interface. This suggests that the surface stress and surface electric displacement jumps exist across the interface whereas the mechanical displacement and electric potential are continuous. The bulk material is a transversely isotropic piezoelectric solid, embedding cylindrical porosities with circular cross-sectional shape. The porosities have the same radius. Along the pore boundary, the surface stress and surface electric displacement prevail. The constitutive behavior of the interface is described by the extended Gurtin--Murdoch interface model (Chen, 2008). Based on the composite cylinder assemblage model and the generalized self-consistent scheme, closed-form solutions are derived to exactly obtain the homogenized Hill's moduli, piezoelectric and dielectric constants. In the analytical approaches, the variation of surface stress and electric displacement is governed by the generalized Young--Laplace condition considering the stress equilibrium and charge conservation equations (Chen et al., 2006). Additionally, the zeroth-order asymptomatic multiphysics finite-element micromechanics enhanced with surface piezoelectricity is developed for the first time, wherein the surface piezoelectricity is incorporated directly by additional surface energy associated with the elements that are situated along the pore boundary. The accuracy of the developed approaches is then extensively verified and critically assessed over a broad variety of parameters and dimensions.

It is the goal of the present work to demonstrate that the widely-accepted classical micromechanics models such as the CCA and GSCM remain useful tools in predicting effective properties of piezoelectric nanocomposites with surface piezoelectricity. The differential coated cylinder assemblages (DCCA) have also been explored by (Lefèvre and Lopez-Pamies, 2015) in

order to compute the effective properties of a single class of composites. It should be noted that the current manuscript focuses only on the kinematically coherent interface. Introducing the more complicated general interface model would increase the complexity of the problem by introducing mechanical displacement and electric potential discontinuities and bring more parameters that need to be identified, leading to distractions from the fundamental theoretical framework developed in this manuscript. Such extensions will be explored in our future work.

The rest of the manuscript is structured as follows: Section 2 recalls the extended coherent interface model with surface piezoelectricity and the homogenization theory in the presence of a coherent interface. Section 3 presents the extension of the CCA/GSCM accounting for surface piezoelectricity. The theoretical development of the multiphysics FEM with energetic surfaces is demonstrated in Section 4. Comparisons of the extended CCA/GSCM and multiphysics FEM, as well as the numerical instabilities in the unit cell solution encountered when the interface energies are negative, are discussed in Section 5. Section 6 draws pertinent conclusions. The FEM and exact solution of electric displacement fields for the generalized Kirsch problems are compared in the Appendix.

2. Preliminaries

The scope of this section is to define the problem under consideration. Hereafter, some preliminary notes concerning the extended coherent interface model and the homogenization theory in the presence of surface piezoelectricity are recalled.

2.1 Coherent Interface Model with Surface Piezoelectricity

Figure 1a depicts a sketch of unidirectional piezoelectric nanocomposites, in the Cartesian coordinates $\left(x,y,z\right)$ or in the cylindrical coordinates $\left(r,\theta,z\right)$, containing circular porosities of

the same radii which are dispersed randomly or placed periodically in the $x-y$ plane. The constitutive relation for a linear piezoelectric bulk material under the infinitesimal regime of deformations and rotations reads (Chen, 2008):

$$\begin{aligned}\boldsymbol{\sigma} &= \mathbf{C}\cdot\boldsymbol{\varepsilon} + \mathbf{e}\cdot\left[-\mathbf{E}\right] \\ \mathbf{D} &= \mathbf{e}^{\mathrm{T}}\cdot\boldsymbol{\varepsilon} - \boldsymbol{\kappa}\cdot\left[-\mathbf{E}\right]\end{aligned} \tag{1}$$

where $\boldsymbol{\sigma}=\left[\sigma_{rr},\sigma_{\theta\theta},\sigma_{zz},\sigma_{z\theta},\sigma_{rz},\sigma_{r\theta}\right]^{\mathrm{T}}$ denote stresses, $\boldsymbol{\varepsilon}=\left[\varepsilon_{rr},\varepsilon_{\theta\theta},\varepsilon_{zz},2\varepsilon_{z\theta},2\varepsilon_{rz},2\varepsilon_{r\theta}\right]^{\mathrm{T}}$ denote strains, $\mathbf{D}=\left[D_r,D_\theta,D_z\right]^{\mathrm{T}}$ denote electric displacements, $\mathbf{E}=\left[E_r,E_\theta,E_z\right]^{\mathrm{T}}$ denote electric fields. The elastic modulus $\mathbf{C}$, piezoelectric constant $\mathbf{e}$, and dielectric constant $\boldsymbol{\kappa}$ are the fourth-rank, third-rank, and second-rank tensors, respectively. In the case of transversely isotropic phase with the axis of symmetry parallel to the z axis (Chen, 2008),

$$\mathbf{C}=\begin{bmatrix} k+m & k-m & l & 0 & 0 & 0 \\ k-m & k+m & l & 0 & 0 & 0 \\ l & l & n & 0 & 0 & 0 \\ 0 & 0 & 0 & p & 0 & 0 \\ 0 & 0 & 0 & 0 & p & 0 \\ 0 & 0 & 0 & 0 & 0 & m \end{bmatrix},\quad \mathbf{e}=\begin{bmatrix} 0 & 0 & e_{31} \\ 0 & 0 & e_{31} \\ 0 & 0 & e_{33} \\ 0 & e_{15} & 0 \\ e_{15} & 0 & 0 \\ 0 & 0 & 0 \end{bmatrix},\quad \boldsymbol{\kappa}=\begin{bmatrix} \kappa_{11} & 0 & 0 \\ 0 & \kappa_{11} & 0 \\ 0 & 0 & \kappa_{33} \end{bmatrix} \tag{2}$$

where k, l, n, m and p denote the Hill's elastic moduli respectively for plane strain bulk modulus, cross modulus, unit uniaxial straining modulus, transverse shear modulus, and axial shear modulus (Hill, 1964). The piezoelectric tensor is characterized by three constants e_{31}, e_{33} and e_{15} while the dielectric tensor is defined by two constants κ_{11} and κ_{33}.

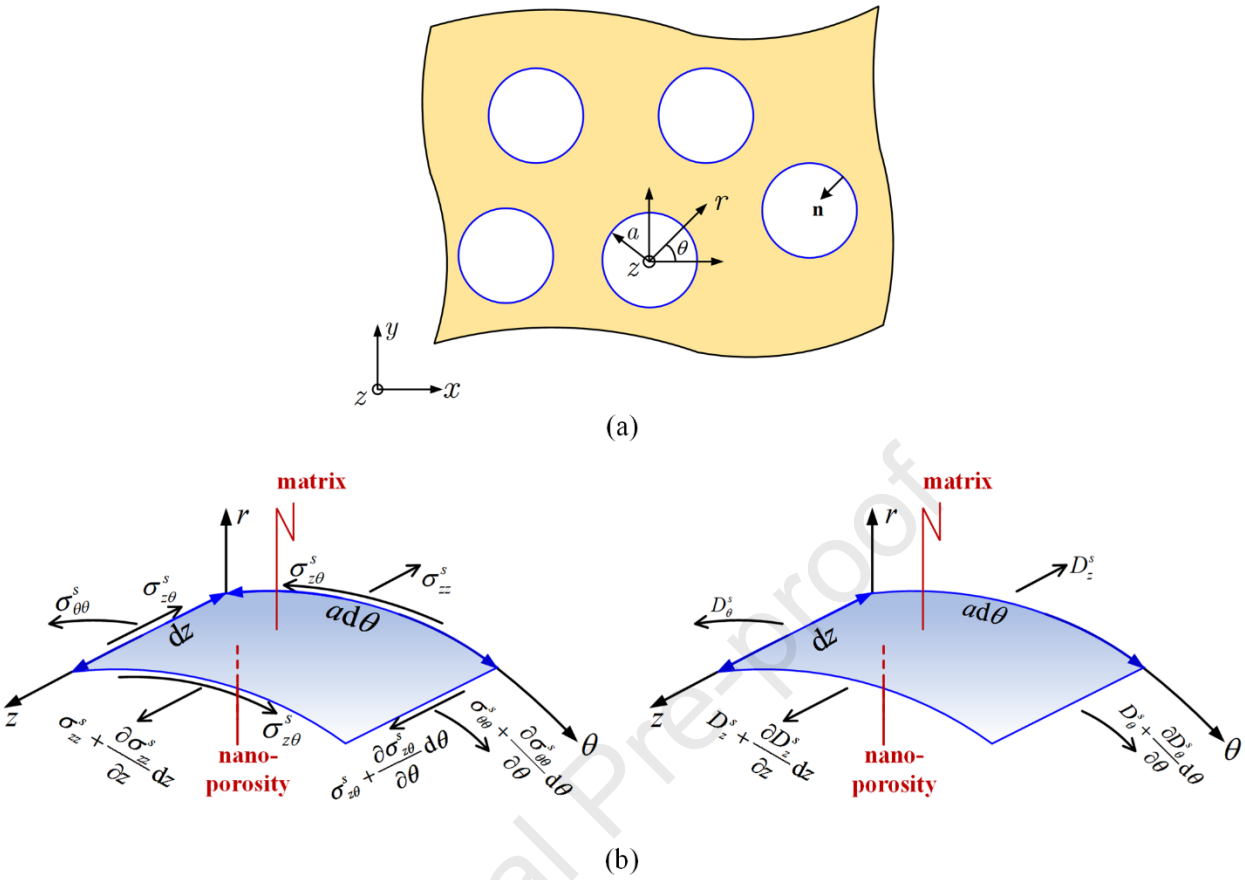

Figure 1(a) A schematic illustration of unidirectional nanoporous materials with pore radius of a ; (b) A schematic illustration of an infinitesimally thin surface with a constant curvature, illustrating the variation of surface stress and electric displacement balanced by the traction and electric displacement on the matrix side of the interface of a porous nanocomposite according to the Young--Laplace equations

In addition to the bulk materials, energetic surfaces are considered that stretch along the pore boundaries. In nanoscale piezoelectric solids, the idea is based on the notion that the interface stresses can be modelled as three in-plane stresses, $\sigma^s_{\theta\theta}$, σ^s_{zz} and $\sigma^s_{z\theta}$, along the tangent planes of a curved interface, as shown in Figure 1b, which can be described by the coherent interface model developed by Gurtin and Murdoch (1975, 1978). In this model, the surface is viewed as a two-dimensional, infinitesimally thin sheet with its own material properties. In Chen (2008), the effect of surface electric displacements, D^s_θ and D^s_z, has been added to the linear version of Gurtin--Murdoch surface elasticity theory. The interfacial stress and electric displacement variations are governed by the interface stress equilibrium and charge conservation equations, respectively,

which describe the jump condition of the stress vectors and electric displacement taken from the bulk neighborhood. This is also known as the generalized Young--Laplace equation, Chen et al. (2006). For an interface separating the inclusion with a constant radius a and the surrounding bulk materials, the generalized Young--Laplace equation in the cylindrical coordinates reads:

$$\sigma_{rr} = \frac{\sigma^s_{\theta\theta}}{a}, \quad \sigma_{r\theta} = -\left(\frac{1}{a}\frac{\partial \sigma^s_{\theta\theta}}{\partial \theta} + \frac{\partial \sigma^s_{z\theta}}{\partial z}\right), \quad \sigma_{rz} = -\left(\frac{\partial \sigma^s_{zz}}{\partial z} + \frac{1}{a}\frac{\partial \sigma^s_{\theta z}}{\partial \theta}\right), \quad D_r = -\left(\frac{1}{a}\frac{\partial D^s_{\theta}}{\partial \theta} + \frac{\partial D^s_{z}}{\partial z}\right) \tag{3}$$

where " " denotes stress and electric displacement jumps along the two sides of the interface. In the case of vanishing inclusion, the σ_{rr}, $\sigma_{r\theta}$, σ_{rz} and D_r are the stresses and electric displacement evaluated along $r = a$ at the bulk material side. $\sigma^s_{\theta\theta}$, $\sigma^s_{z\theta}$, σ^s_{zz}, D^s_{θ} and D^s_z are the stresses and electric displacements associated with the energetic surfaces. It should be noted that, for an infinite-long porosity, the terms $\partial/\partial z$ in Eq. (3) vanish as there are no variations of surface stress and electric displacement in the axial direction. The above equations replace the traction-free and electric-displacement-free conditions at the pore boundaries in the classical boundary value problems without surface energy effects. The constitutive relation of the infinitesimally thin interface, under the generalized plane stress assumption, can be expressed as (Chen, 2008):

$$\begin{aligned} \boldsymbol{\sigma}^s &= \mathbf{C}^s \cdot \boldsymbol{\varepsilon}^s + \mathbf{e}^s \cdot \left[-\mathbf{E}^s\right] \\ \mathbf{D}^s &= \mathbf{e}^{s\mathrm{T}} \cdot \boldsymbol{\varepsilon}^s - \boldsymbol{\kappa}^s \cdot \left[-\mathbf{E}^s\right] \end{aligned} \tag{4}$$

where $\boldsymbol{\sigma}^s = \left[0, \sigma^s_{\theta\theta}, \sigma^s_{zz}, \sigma^s_{z\theta}, 0, 0\right]^{\mathrm{T}}$, $\boldsymbol{\varepsilon}^s = \left[0, \varepsilon^s_{\theta\theta}, \varepsilon^s_{zz}, 2\varepsilon^s_{z\theta}, 0, 0\right]^{\mathrm{T}}$, $\mathbf{D}^s = \left[0, D^s_{\theta}, D^s_z\right]^{\mathrm{T}}$, $\mathbf{E}^s = \left[0, E^s_{\theta}, E^s_z\right]^{\mathrm{T}}$, and

$$\mathbf{C}^s=\begin{bmatrix}0&0&0&0&0&0\\0&c_{11}^s&c_{13}^s&0&0&0\\0&c_{13}^s&c_{33}^s&0&0&0\\0&0&0&c_{44}^s&0&0\\0&0&0&0&0&0\\0&0&0&0&0&0\end{bmatrix},\quad \mathbf{e}^s=\begin{bmatrix}0&0&0\\0&0&e_{31}^s\\0&0&e_{33}^s\\0&e_{15}^s&0\\0&0&0\\0&0&0\end{bmatrix},\quad \boldsymbol{\kappa}^s=\begin{bmatrix}0&0&0\\0&\kappa_{11}^s&0\\0&0&\kappa_{33}^s\end{bmatrix} \tag{5}$$

where c_{ij}^s are the surface elastic moduli, e_{ijk}^s denote the surface piezoelectric constants, and $\boldsymbol{\kappa}_{ij}^s$ represent the surface dielectric constants. These surface properties are typically determined by atomistic simulations (Dai et al., 2011; Miller and Shenoy, 2000; Shenoy, 2005). In this manuscript, due to the lack of such data, we adopt a phenomenological perspective and assume the surface properties to be known quantities. It should be mentioned that the dimensions of stress and electric displacement in the energetic surfaces are force or electric charge per unit length, respectively, which are not the same as those in the bulk material, namely, force or electric charge per unit area, respectively. The difference in the units of stress and electric displacement is due to zero-thickness nature of the interface and is depicted in the Young--Laplace equation. In addition, the coherency of the interface requires that tangential and longitudinal components of the strain and electric field are continuous across the interface, namely:

$$\varepsilon_{\theta\theta}^s=\varepsilon_{\theta\theta},\quad \varepsilon_{z\theta}^s=\varepsilon_{z\theta},\quad \varepsilon_{zz}^s=\varepsilon_{zz},\quad E_\theta^s=E_\theta,\quad E_z^s=E_z \tag{6}$$

where strain and electric field components without superscript s are the quantities evaluated at $r=a$ of the bulk material side.

2.2 Homogenized Constitutive Relations

Following the classical homogenization theory, the homogenized constitutive relations of the nanoporous piezoelectric materials can be expressed in terms of effective constants, designated by

an asterisk, that relate the macroscopic strain $\bar{\boldsymbol{\varepsilon}}$ and electric field $\bar{\mathbf{E}}$ vectors to the macroscopic stress $\bar{\boldsymbol{\sigma}}$ and electric displacement $\bar{\mathbf{D}}$ vectors as follows:

$$\begin{aligned}\bar{\boldsymbol{\sigma}} &= \mathbf{C}^{*}\cdot\bar{\boldsymbol{\varepsilon}} + \mathbf{e}^{*}\cdot\left[-\bar{\mathbf{E}}\right] \\ \bar{\mathbf{D}} &= \mathbf{e}^{*\mathrm{T}}\cdot\bar{\boldsymbol{\varepsilon}} - \boldsymbol{\kappa}^{*}\cdot\left[-\bar{\mathbf{E}}\right]\end{aligned} \tag{7}$$

In the above equations, the macroscopic strain and electric field are computed directly by the classical volume-averaging of their local quantities as follows:

$$\bar{\varepsilon}_{ij} = \frac{1}{V}\int_V \varepsilon_{ij}\,\mathrm{d}V, \quad \bar{E}_i = \frac{1}{V}\int_V E_i\,\mathrm{d}V \tag{8}$$

where V denotes the total volume over the entire representative volume element or repeating unit cell. In contrast, the effective stress and electric displacement, in the presence of surface stress and electric displacement, are evaluated using the divergence theory (Chatzigeorgiou et al., 2015b; Ghosh and Lopez-Pamies, 2022) in the following form:

$$\bar{\sigma}_{ij} = \frac{1}{V}\int_V \sigma_{ij}\,\mathrm{d}V + \frac{1}{V}\int_S \sigma^{s}_{ij}\,\mathrm{d}S, \quad \bar{D}_i = \frac{1}{V}\int_V D_i\,\mathrm{d}V + \frac{1}{V}\int_S D^{s}_i\,\mathrm{d}S \tag{9}$$

3. Generalized CCA/GSCM Model with Surface Piezoelectricity

In this section, the composite cylinder assemblage model, developed by Hashin and Rosen (1964), and the generalized self-consistent model, developed by Christensen and Lo (1979), are further extended to model the nanoporous piezoelectric materials, enhanced with surface piezoelectricity. Following Chatzigeorgiou et al. (2019a; 2019b), to obtain a complete set of effective properties of such composites, three different loading modes may be identified, including (a) combined radial tension, axial tension, and axial electric field loading; (b) combined axial shear and transverse electric field loading; (c) transverse shear loading as follows:

3.1 Axisymmetric moduli k^*, l^*, n^*, piezoelectric and dielectric constants e_{31}^*, e_{33}^*, κ_{33}^*

The axisymmetric moduli k^*, l^*, n^* and piezoelectric properties e_{31}^*, e_{33}^*, κ_{33}^* defined for transversely isotropic materials are obtained under the axisymmetric loading $\bar{\varepsilon}_{xx} = \bar{\varepsilon}_{yy}$ with the generalized plane strain constraint $\varepsilon_{zz} = \bar{\varepsilon}_{zz}$ and $E_z = \bar{E}_z$, which produces $\bar{\sigma}_{xx} = \bar{\sigma}_{yy}$ in the Cartesian coordinates. Using the strain and stress transformation equations, $\bar{\varepsilon}_{rr} = \bar{\varepsilon}_{\theta\theta}$ and $\bar{\sigma}_{rr} = \bar{\sigma}_{\theta\theta}$ are obtained. In this regard, the generalized homogenized Hooke's law in the cylindrical coordinates for this loading reads:

$$\begin{bmatrix} \bar{\sigma}_{rr} \\ \bar{\sigma}_{zz} \\ \bar{D}_z \end{bmatrix} = \begin{bmatrix} 2k^* & l^* & e_{31}^* \\ 2l^* & n^* & e_{33}^* \\ 2e_{31}^* & e_{33}^* & -\kappa_{33}^* \end{bmatrix} \begin{bmatrix} \bar{\varepsilon}_{rr} \\ \bar{\varepsilon}_{zz} \\ -\bar{E}_z \end{bmatrix} \tag{10}$$

From the above equation, it is noted that to obtain the complete set of the homogenized properties under axisymmetric loading, one can sequentially apply only one unit macroscopic strain component $\bar{\varepsilon}_{rr}$ and $\bar{\varepsilon}_{zz}$, or electric field $\bar{E}_z$ to iteratively solve Eq. (10) to obtain the associated stress field and electric displacement, which yields the corresponding homogenized properties in each column of the generalized stiffness matrix.

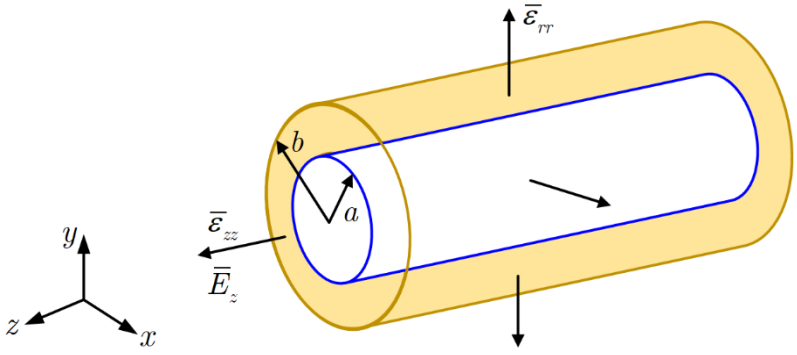

Figure 2 Combined longitudinal tension, longitudinal electric field, and all-around tension loading

In the case of a nanocomposite comprised of an infinitely-long cylindrical cavity of radius a embedded in a matrix annulus of radius b, which is subjected to uniform all-around tension or compression in the radial direction expressed in terms of the imposed uniform strain $\bar{\varepsilon}_{rr} = \varepsilon_{rr}^{o}$ under the generalized plane strain constraint $\varepsilon_{zz} = \bar{\varepsilon}_{zz}$ and $E_z = \bar{E}_z$, the displacement field and electric potential can be expressed as:

$$u_r = \left(\Xi_1 + \Xi_2 r^{-2}\right) r, \quad u_\theta = 0, \quad u_z = \Xi_3 z, \quad \phi = -\Xi_4 z \tag{11}$$

which produce the following strains and electric field upon using the strain-displacement and electric potential-electric field relations,

$$\varepsilon_{rr} = \Xi_1 - \Xi_2 r^{-2}, \quad \varepsilon_{\theta\theta} = \Xi_1 + \Xi_2 r^{-2}, \quad \varepsilon_{zz} = \Xi_3, \quad E_z = \Xi_4 \tag{12}$$

where Ξ_i ($i = 1, 2, 3, 4$) are the unknown constants. These general expressions lead to the stresses and electric displacements that satisfy the equilibrium and charge conservation equation. We note that the expressions for the radial and tangential displacements are similar to those in a thick-walled cylinder subject to internal and/or external pressure based on the classical linear elasticity theory.

Subsequently, the radial and axial stresses in the bulk materials, as well as the energetic hoop, axial stresses and axial electric displacement, are expressed in terms of the unknown constants and surface and bulk properties upon the use of the generalized Hooke's law under the generalized plane strain condition:

$$\begin{aligned}
\sigma_{rr} &= 2k\Xi_1 - 2mr^{-2}\Xi_2 + l\Xi_3 - e_{31}\Xi_4 \\
\sigma_{zz} &= 2l\Xi_1 + n\Xi_3 - e_{33}\Xi_4 \\
\sigma^s_{\theta\theta} &= c^s_{11}\Xi_1 + c^s_{11}a^{-2}\Xi_2 + c^s_{13}\Xi_3 - e^s_{31}\Xi_4 \\
\sigma^s_{zz} &= c^s_{13}\Xi_1 + c^s_{13}a^{-2}\Xi_2 + c^s_{33}\Xi_3 - e^s_{33}\Xi_4 \\
D^s_z &= e^s_{31}\Xi_1 + e^s_{31}a^{-2}\Xi_2 + e^s_{33}\Xi_3 + \kappa^s_{33}\Xi_4
\end{aligned} \tag{13}$$

The unknown constants Ξ_i are obtained from the boundary condition and the extended Young--Laplace equation. Specifically, the homogenized displacement boundary condition imposed at $r=b$ under the generalized plane strain constraint reads:

$$u_r(b)=\bar{\varepsilon}_{rr}b,\quad \varepsilon_{zz}=\bar{\varepsilon}_{zz},\quad E_z=\bar{E}_z \tag{14}$$

The Young--Laplace equation for the radial stress is expressed as:

$$\sigma_{rr}(a)=\frac{\sigma^s_{\theta\theta}}{a} \tag{15}$$

It should be noted that the Young--Laplace equation for the radial electric displacement is automatically satisfied under the axisymmetric loading path hence the radial electric displacement jump condition is omitted herein.

Finally, the global system of equations for the determination of the unknown constants expressed in terms of the macroscopic strain and electric field are obtained as:

$$\begin{bmatrix} 1 & b^{-2} & 0 & 0 \\ 0 & 0 & 1 & 0 \\ 0 & 0 & 0 & 1 \\ 2k-c^s_{11}a^{-1} & -\left(2m+c^s_{11}a^{-3}\right) & l-c^s_{13}a^{-1} & -\left(e_{31}-e^s_{31}a^{-1}\right) \end{bmatrix}\begin{bmatrix} \Xi_1 \\ \Xi_2 \\ \Xi_3 \\ \Xi_4 \end{bmatrix}=\begin{bmatrix} \bar{\varepsilon}_{rr} \\ \bar{\varepsilon}_{zz} \\ \bar{E}_z \\ 0 \end{bmatrix} \tag{16}$$

3.2 Axial shear modulus p^*, the in-plane piezoelectric and dielectric constants e^*_{15}, κ^*_{11}

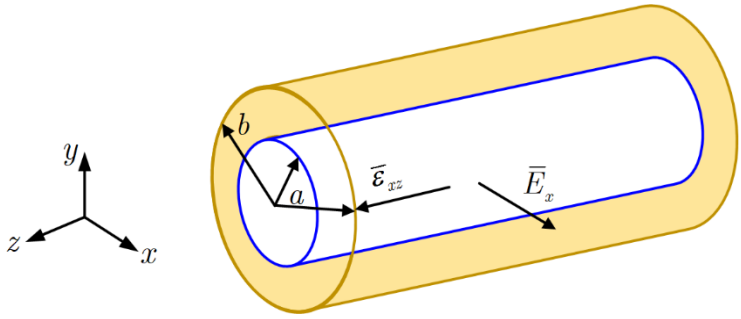

Figure 3 Combined axial shear and transverse electric field loading

For this loading case, the following displacement and electric potential are applied:

$$u_z = 2\bar{\varepsilon}_{zx} x, \quad \phi = -\bar{E}_x x \tag{17}$$

which yield the following generalized homogenized Hooke's law for the axial shear and in-plane electric field loading:

$$\begin{bmatrix} \bar{\sigma}_{zx} \\ \bar{D}_x \end{bmatrix} = \begin{bmatrix} p^* & e_{15}^* \\ e_{15}^* & -\kappa_{11}^* \end{bmatrix} \begin{bmatrix} 2\bar{\varepsilon}_{zx} \\ -\bar{E}_x \end{bmatrix} \tag{18}$$

In the cylindrical coordinates, upon the use of the coordinate transformation relation, Eq. (17) at $r = b$ becomes:

$$u_z(b,\theta) = 2\bar{\varepsilon}_{zx} b\cos\theta, \quad \phi(b,\theta) = -\bar{E}_x b\cos\theta \tag{19}$$

The equilibrium and Maxwell conservation equations under the combined axial shear and transverse electric field loading given in terms of displacement and electric potential read:

$$\begin{aligned} p\left(\frac{\partial^2 u_z}{\partial r^2} + \frac{1}{r}\frac{\partial u_z}{\partial r} + \frac{1}{r^2}\frac{\partial^2 u_z}{\partial \theta^2}\right) + e_{15}\left(\frac{\partial^2 \phi}{\partial r^2} + \frac{1}{r}\frac{\partial \phi}{\partial r} + \frac{1}{r^2}\frac{\partial^2 \phi}{\partial \theta^2}\right) = 0 \\ e_{15}\left(\frac{\partial^2 u_z}{\partial r^2} + \frac{1}{r}\frac{\partial u_z}{\partial r} + \frac{1}{r^2}\frac{\partial^2 u_z}{\partial \theta^2}\right) - \kappa_{11}\left(\frac{\partial^2 \phi}{\partial r^2} + \frac{1}{r}\frac{\partial \phi}{\partial r} + \frac{1}{r^2}\frac{\partial^2 \phi}{\partial \theta^2}\right) = 0 \end{aligned} \tag{20}$$

By solving Eq. (20), the displacement u_z and electric potential ϕ accounting for the boundary conditions in Eq. (19) are obtained as:

$$\begin{aligned} u_z(r,\theta) &= \left(\Xi_1 + \Xi_2 r^{-2}\right) r\cos\theta \\ \phi(r,\theta) &= \left(\Xi_3 + \Xi_4 r^{-2}\right) r\cos\theta \end{aligned} \tag{21}$$

which produce shear strain and electric field in the following form:

$$\begin{aligned} 2\varepsilon_{zr} &= \left(\Xi_1 - \Xi_2 r^{-2}\right)\cos\theta \\ 2\varepsilon_{z\theta} &= -\left(\Xi_1 + \Xi_2 r^{-2}\right)\sin\theta \\ E_r &= -\left(\Xi_3 - \Xi_4 r^{-2}\right)\cos\theta \\ E_\theta &= \left(\Xi_3 + \Xi_4 r^{-2}\right)\sin\theta \end{aligned} \tag{22}$$

where Ξ_i ($i = 1,2,3,4$) are the unknown constants.

The shear stress and radial electric displacement in the bulk materials, together with the energetic interface shear stress and hoop electric are obtained in terms of the unknown constants, the surface and bulk properties in the following form:

$$\begin{aligned}
\sigma_{zr} &= p\left(\Xi_1 - \Xi_2 r^{-2}\right)\cos\theta + e_{15}\left(\Xi_3 - \Xi_4 r^{-2}\right)\cos\theta \\
D_r &= e_{15}\left(\Xi_1 - \Xi_2 r^{-2}\right)\cos\theta - \kappa_{11}\left(\Xi_3 - \Xi_4 r^{-2}\right)\cos\theta \\
\sigma^s_{\theta z} &= -c^s_{44}\left(\Xi_1 + \Xi_2 r^{-2}\right)\sin\theta - e^s_{15}\left(\Xi_3 + \Xi_4 r^{-2}\right)\cos\theta \\
D^s_{\theta} &= -e^s_{15}\left(\Xi_1 + \Xi_2 r^{-2}\right)\sin\theta + \kappa^s_{11}\left(\Xi_3 + \Xi_4 r^{-2}\right)\sin\theta
\end{aligned} \tag{23}$$

The unknown constants Ξ_i are obtained from the boundary conditions Eq. (19) and the generalized Young--Laplace equations as follows:

$$\begin{aligned}
\sigma_{rz}(a,\theta) &= -\frac{1}{a}\frac{\partial \sigma^s_{\theta z}}{\partial \theta} \\
D_r(a,\theta) &= -\frac{1}{a}\frac{\partial D^s_{\theta}}{\partial \theta}
\end{aligned} \tag{24}$$

noting that $\partial \sigma^s_{zz}/\partial z = 0$ and $\partial D^s_z/\partial z = 0$, which yield the following system of equations for the determination of the unknown constants:

$$\begin{bmatrix}
1 & b^{-2} & 0 & 0 \\
0 & 0 & 1 & b^{-2} \\
p - c^s_{44}a^{-1} & -\left(pa^{-2} + c^s_{44}a^{-3}\right) & e_{15} - e^s_{15}a^{-1} & -\left(e_{15}a^{-2} + e^s_{15}a^{-3}\right) \\
e_{15} - e^s_{15}a^{-1} & -\left(e_{15}a^{-2} + e^s_{15}a^{-3}\right) & -\kappa_{11} + \kappa^s_{11}a^{-1} & \kappa_{11}a^{-2} + \kappa^s_{11}a^{-3}
\end{bmatrix}
\begin{bmatrix} \Xi_1 \\ \Xi_2 \\ \Xi_3 \\ \Xi_4 \end{bmatrix} =
\begin{bmatrix} 2\bar{\varepsilon}_{zx} \\ -\bar{E}_x \\ 0 \\ 0 \end{bmatrix} \tag{25}$$

3.3 Transverse shear modulus m^*

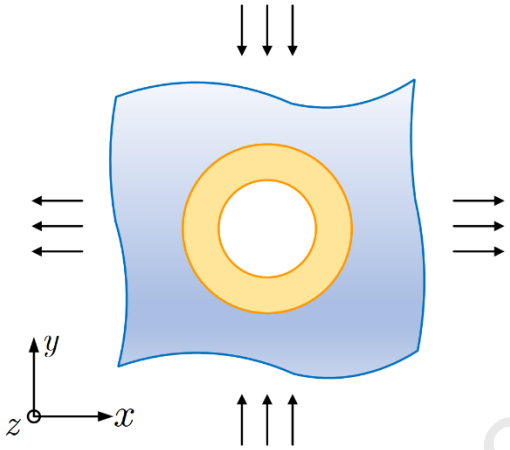

Figure 4 Transverse shear loading

The analytical solution for the transverse effective shear modulus m^* cannot be obtained directly for the CCA model because the equivalence between homogeneous displacement and traction boundary conditions no longer holds for a single composite cylinder. Therefore, the GSCM model (including the fiber, matrix, and effective medium) has been considered to compute the effective properties under transverse shear loading for nanocomposites with an energetic surface (Chen et al., 2018b). Herein, the three-phase model will be further simplified to model real porosity with surface piezoelectricity. For this loading case, the biaxial tension-compression far-field loading is applied as follows:

$$\varepsilon_{xx}^{\infty} = -\varepsilon_{yy}^{\infty} = \varepsilon^{o} \tag{26}$$

The displacement fields in the matrix and effective medium are given in the following form (Christensen and Lo, 1979):

For $a \le r \le b$

$$\begin{aligned} u_r^m(r,\theta) &= \left[\Xi_1(\eta-3)r^3 + \Xi_2 r + \Xi_3(\eta+1)r^{-1} + \Xi_4 r^{-3}\right]\cos 2\theta \\ u_\theta^m(r,\theta) &= \left[\Xi_1(\eta+3)r^3 - \Xi_2 r - \Xi_3(\eta-1)r^{-1} + \Xi_4 r^{-3}\right]\sin 2\theta \end{aligned} \tag{27}$$

For $r \ge b$

$$
\begin{aligned}
u_r^c(r,\theta) &= \left[\Xi_5 r + \Xi_6\left(\eta^* + 1\right) r^{-1} + \Xi_7 r^{-3}\right]\cos 2\theta \\
u_\theta^c(r,\theta) &= \left[-\Xi_5 r - \Xi_6\left(\eta^* - 1\right) r^{-1} + \Xi_7 r^{-3}\right]\sin 2\theta
\end{aligned}
\tag{28}
$$

where $\Xi_i\left(i=1,...,7\right)$ are the unknown coefficients to be determined. $\eta = 1+2m/k$ and $\eta^* = 1+2m^*/k^*$.

The far-field loading expressed in terms of displacements in the Cartesian coordinates reads:

$$
u_x = \varepsilon^o x, \quad u_y = -\varepsilon^o y \tag{29}
$$

In the cylindrical coordinates, the above equation becomes:

$$
\lim_{r\to\infty} u_r(r,\theta) = \varepsilon^o r\cos 2\theta, \quad \lim_{r\to\infty} u_\theta(r,\theta) = -\varepsilon^o r\sin 2\theta \tag{30}
$$

To determine the unknown coefficients in Eqs. (27) and (28), the generalized Young--Laplace equation and continuity condition at the matrix/composite interface are enforced:

$$
\begin{aligned}
\sigma_{rr}^m(a,\theta) &= \frac{\sigma_{\theta\theta}^s}{a} \\
\sigma_{r\theta}^m(a,\theta) &= -\frac{1}{a}\frac{\partial\sigma_{\theta\theta}^s}{\partial\theta} \\
u_r^m(b,\theta) &= u_r^c(b,\theta) \\
u_\theta^m(b,\theta) &= u_\theta^c(b,\theta) \\
\sigma_{rr}^m(b,\theta) &= \sigma_{rr}^c(b,\theta) \\
\sigma_{r\theta}^m(b,\theta) &= \sigma_{r\theta}^c(b,\theta)
\end{aligned}
\tag{31}
$$

noting that $\partial\sigma_{z\theta}^s/\partial z = 0$. In addition, the Eshelby formula states that for a homogeneous medium containing an inclusion, the strain energy under applied displacement conditions is the same as that of the same medium when it contains no inclusion, which leads to the following condition to be satisfied:

$$
\int_{S_{r=b}} \left(\sigma_{rr}^c u_r^0 + \sigma_{r\theta}^c u_\theta^0 - \sigma_{rr}^0 u_r^c - \sigma_{r\theta}^0 u_\theta^c\right) b\,\mathrm{d}\theta = 0 \tag{32}
$$

where $\sigma_{rr}^0 = \cos 2\theta, \sigma_{r\theta}^0 = -\sin 2\theta$ and $u_r^0 = \frac{b}{2m^*}\cos 2\theta, u_\theta^0 = -\frac{b}{2m^*}\sin 2\theta$ denote the stresses and displacements in the medium when it contains no inclusion, respectively. For detailed derivation, see Christensen and Lo (1979). Solution of Eqs. (30)-(32) yields the quadratic expression for the determination of the effective transverse shear modulus m^*. It should be pointed out that using the differential coated cylinder assemblages (DCCA) approach for all the properties renders similar results for the effective properties (see Lefèvre and Lopez-Pamies, 2015; Milton, 1985).

4. Finite-Element Asymptotic Homogenization Accounting for Surface Piezoelectricity

In this section, following the work by (Cavalcante et al., 2011; Chen et al., 2019; Chen and Wang, 2020; Saeb et al., 2016), the multiphysics finite-element micromechanics homogenization theory accounting for the surface piezoelectricity is developed for studying the size-dependent behavior in nanoporous piezoelectric materials for the first time.

In the same spirit as the asymptotic expansion theory widely used in the homogenization of mechanical problems in composites (Bensoussan et al., 1978; He and Pindera, 2021a, b), the displacement and electric potential fields in the q th element are represented by the two-scale expansion involving the macroscopic coordinates **x** and the microscopic coordinates **y** of the following form:

$$\begin{aligned} u_i^{(q)} &= \bar{\varepsilon}_{ij} x_j + u_i'^{(q)} \\ \phi^{(q)} &= -\bar{E}_i x_i + \phi'^{(q)} \end{aligned} \tag{33}$$

where $i = 1, 2, 3$, $\bar{\varepsilon}_{ij}$ are the applied macroscopic strains and $\bar{E}_i$ are the applied electric field. $u_i'^{(q)}$ and $\phi'^{(q)}$ denote the fluctuating displacement and electric potential fields induced by the microstructures, which are approximated directly in terms of nodal quantities, $\mathbf{u}'^{o(q)}$ and $\Phi'^{o(q)}$,

and interpolation functions. Accordingly, the microscopic strain $\varepsilon_{ij}^{(q)}$ and electric fields $E_i^{(q)}$ are obtained in terms of macroscopic and fluctuating components as follows:

$$\begin{aligned}\varepsilon_{ij}^{(q)} &= \bar{\varepsilon}_{ij} + \varepsilon_{ij}'^{(q)} = \bar{\varepsilon}_{ij} + \frac{1}{2}\left(\frac{\partial u_i'}{\partial y_j} + \frac{\partial u_j'}{\partial y_i}\right)^{(q)} \\ E_i^{(q)} &= \bar{E}_i + E_i'^{(q)} = \bar{E}_i - \frac{\partial \phi'^{(q)}}{\partial y_i}\end{aligned} \tag{34}$$

Applying the differential operators to the fluctuating displacement and electric potential, the fluctuating strain and electric fields are obtained in the following form:

$$\begin{aligned}\boldsymbol{\varepsilon}'^{(q)} &= \mathbf{B}_u^{(q)} \mathbf{u}'^{o(q)} \\ \mathbf{E}'^{(q)} &= -\mathbf{B}_\phi^{(q)} \Phi'^{o(q)}\end{aligned} \tag{35}$$

where $\mathbf{u}'^{o(q)} = \left[\mathbf{u}'^{(1)} ... \mathbf{u}'^{(N)}\right]^{\mathrm{T}}$ with $\mathbf{u}'^{(p)} = \left[u_1', u_2', u_3'\right]^{o(p)\mathrm{T}}$, $\Phi'^{o(q)} = \left[\phi'^{(1)}, ..., \phi'^{(N)}\right]^{\mathrm{T}}$, N denotes the total number of nodes in q th element. $\mathbf{B}_u^{(q)}$ denotes the strain-displacement matrix and $\mathbf{B}_\phi^{(q)}$ denotes the electric field-electric potential matrix, which are used to construct the potential energy integral at the element level (Chen and Wang, 2020).

Before passing to the actual boundary value problem, it is essential to express all the fields and constitutive laws, namely Eqs. (1) and (4), in Cartesian coordinates. The axes in the Cartesian $\left(x_1, x_2, x_3\right)$ and cylindrical $\left(r, \theta, z\right)$ coordinates are linked through the following relation:

$$x_1 = r\cos\theta, \quad x_2 = r\sin\theta, \quad x_3 = z \tag{36}.$$

Accordingly, the stress, strain, electric displacement, and electric field vectors in Voigt notation are transformed between the cylindrical (indicated by the tilde symbol) and Cartesian coordinate systems:

$$\begin{aligned}&\tilde{\boldsymbol{\varepsilon}} = \mathbf{Q}_\varepsilon \cdot \boldsymbol{\varepsilon}, \quad \tilde{\boldsymbol{\sigma}} = \mathbf{Q}_\sigma \cdot \boldsymbol{\sigma}, \quad \boldsymbol{\varepsilon} = \mathbf{Q}_\sigma^{\mathrm{T}} \cdot \tilde{\boldsymbol{\varepsilon}}, \quad \boldsymbol{\sigma} = \mathbf{Q}_\varepsilon^{\mathrm{T}} \cdot \tilde{\boldsymbol{\sigma}}, \\ &\tilde{\mathbf{E}} = \mathbf{R}^{\mathrm{T}} \cdot \mathbf{E}, \quad \tilde{\mathbf{D}} = \mathbf{R}^{\mathrm{T}} \cdot \mathbf{D}, \quad \mathbf{E} = \mathbf{R} \cdot \tilde{\mathbf{E}}, \quad \mathbf{D} = \mathbf{R} \cdot \tilde{\mathbf{D}}\end{aligned} \tag{37}$$

where $\mathbf{R}$ denotes the second-order rotator:

$$\mathbf{R}=\begin{bmatrix}\cos\theta & -\sin\theta & 0\\ \sin\theta & \cos\theta & 0\\ 0 & 0 & 1\end{bmatrix} \tag{38}$$

$\mathbf{Q}_\varepsilon$ and $\mathbf{Q}_\sigma$ are the proper fourth-order rotators that transform the strain and the stress vectors expressed in Voigt notation (Chatzigeorgiou et al., 2018; Chatzigeorgiou et al., 2022), respectively:

$$\mathbf{Q}_\varepsilon=\begin{bmatrix}\cos^2\theta & \sin^2\theta & 0 & 0 & 0 & \frac{1}{2}\sin 2\theta\\ \sin^2\theta & \cos^2\theta & 0 & 0 & 0 & -\frac{1}{2}\sin 2\theta\\ 0 & 0 & 1 & 0 & 0 & 0\\ 0 & 0 & 0 & \cos\theta & -\sin\theta & 0\\ 0 & 0 & 0 & \sin\theta & \cos\theta & 0\\ -\sin 2\theta & \sin 2\theta & 0 & 0 & 0 & \cos 2\theta\end{bmatrix} \tag{39}$$

$$\mathbf{Q}_\sigma=\begin{bmatrix}\cos^2\theta & \sin^2\theta & 0 & 0 & 0 & \sin 2\theta\\ \sin^2\theta & \cos^2\theta & 0 & 0 & 0 & -\sin 2\theta\\ 0 & 0 & 1 & 0 & 0 & 0\\ 0 & 0 & 0 & \cos\theta & -\sin\theta & 0\\ 0 & 0 & 0 & \sin\theta & \cos\theta & 0\\ -\frac{1}{2}\sin 2\theta & \frac{1}{2}\sin 2\theta & 0 & 0 & 0 & \cos 2\theta\end{bmatrix} \tag{40}$$

Given the above rotators, the transformation of the generalized stiffness matrices between the cylindrical and Cartesian coordinates takes the form:

$$\begin{aligned}&\tilde{\mathbf{C}}=\mathbf{Q}_\sigma\cdot\mathbf{C}\cdot\mathbf{Q}_\sigma^{\mathrm{T}},\quad \tilde{\mathbf{e}}=\mathbf{Q}_\sigma\cdot\mathbf{e}\cdot\mathbf{R},\quad \tilde{\boldsymbol{\kappa}}=\mathbf{R}^{\mathrm{T}}\cdot\boldsymbol{\kappa}\cdot\mathbf{R}\\ &\mathbf{C}=\mathbf{Q}_\varepsilon^{\mathrm{T}},\cdot\tilde{\mathbf{C}}\cdot\mathbf{Q}_\varepsilon,\quad \mathbf{e}=\mathbf{Q}_\varepsilon^{\mathrm{T}}\cdot\tilde{\mathbf{e}}\cdot\mathbf{R}^{\mathrm{T}},\quad \boldsymbol{\kappa}=\mathbf{R}\cdot\tilde{\boldsymbol{\kappa}}\cdot\mathbf{R}^{\mathrm{T}}\end{aligned} \tag{41}$$

In contrast with the analytical solutions in the previous section, in which the surface piezoelectricity is incorporated through the generalized Young--Laplace equation, the surface effects in the multiphysics finite-element method are taken into account directly through the

additional surface energies associated with the affected elements stretching along the pore boundary. Therefore, the total potential energy Π of the unit cell contains the strain and electric energies with contributions from the bulk materials U^b and energetic surfaces U^s, along with the work done by the external force and electric charge W:

$$\Pi = U^b + U^s - W = \frac{1}{2}\int_V \left(\boldsymbol{\sigma}^{\mathrm{T}} \cdot \boldsymbol{\varepsilon} - \mathbf{D}^{\mathrm{T}} \cdot \mathbf{E}\right) \mathrm{d}V + \frac{1}{2}\int_S \left(\boldsymbol{\sigma}^{s\mathrm{T}} \cdot \boldsymbol{\varepsilon} - \mathbf{D}^{s\mathrm{T}} \cdot \mathbf{E}\right) \mathrm{d}S - \left(\bar{\boldsymbol{\sigma}}^{\mathrm{T}} \cdot \bar{\boldsymbol{\varepsilon}} - \bar{\mathbf{D}}^{\mathrm{T}} \cdot \bar{\mathbf{E}}\right) V \quad (42)$$

The generalized local stiffness matrices are obtained by the minimization of total potential energy Eq.(42), which is done by substituting Eqs. (34) and (35) into Eq. (42) with the help of the generalized Hooke's law in the Cartesian coordinates and then taking the partial derivatives $\partial\Pi/\partial\mathbf{u}' = \mathbf{0}$ and $\partial\Pi/\partial\Phi' = \mathbf{0}$:

$$\left\{\begin{bmatrix} \mathbf{K}_{uu}^b & \mathbf{K}_{u\phi}^b \\ \mathbf{K}_{u\phi}^{\mathrm{bT}} & \mathbf{K}_{\phi\phi}^b \end{bmatrix} + \begin{bmatrix} \mathbf{K}_{uu}^s & \mathbf{K}_{u\phi}^s \\ \mathbf{K}_{u\phi}^{s\mathrm{T}} & \mathbf{K}_{\phi\phi}^s \end{bmatrix}\right\} \begin{bmatrix} \mathbf{u}' \\ \Phi' \end{bmatrix} = \left\{\begin{bmatrix} \mathbf{f}_u^b \\ \mathbf{f}_\phi^s \end{bmatrix} + \begin{bmatrix} \mathbf{f}_u^s \\ \mathbf{f}_\phi^s \end{bmatrix}\right\} \quad (43)$$

where the superscripts b and s denote the contributions from the bulk materials and energetic surface, respectively, with:

$$\begin{aligned}
&\mathbf{K}_{uu}^b = \int_V \mathbf{B}_u^{\mathrm{T}} \cdot \mathbf{C} \cdot \mathbf{B}_u \mathrm{d}V, \quad \mathbf{K}_{\phi\phi}^b = -\int_V \mathbf{B}_\phi^{\mathrm{T}} \cdot \boldsymbol{\kappa} \cdot \mathbf{B}_\phi \mathrm{d}V, \quad \mathbf{K}_{u\phi}^b = \int_V \mathbf{B}_u^{\mathrm{T}} \cdot \mathbf{e} \cdot \mathbf{B}_\phi \mathrm{d}V \\
&\mathbf{K}_{uu}^s = \int_S \mathbf{B}_u^{\mathrm{T}} \cdot \mathbf{C}^s \cdot \mathbf{B}_u \mathrm{d}S, \quad \mathbf{K}_{\phi\phi}^s = -\int_S \mathbf{B}_\phi^{\mathrm{T}} \cdot \boldsymbol{\kappa}^s \cdot \mathbf{B}_\phi \mathrm{d}S, \quad \mathbf{K}_{u\phi}^s = \int_S \mathbf{B}_u^{\mathrm{T}} \cdot \mathbf{e}^{\mathrm{s}} \cdot \mathbf{B}_\phi \mathrm{d}S \\
&\mathbf{f}_u^b = \int_V \left(\mathbf{B}_u^{\mathrm{T}} \cdot \mathbf{e} \cdot \bar{\mathbf{E}} - \mathbf{B}_u^{\mathrm{T}} \cdot \mathbf{C} \cdot \bar{\boldsymbol{\varepsilon}}\right) \mathrm{d}V, \quad \mathbf{f}_\phi^b = -\int_V \left(\mathbf{B}_\phi^{\mathrm{T}} \cdot \mathbf{e}^{\mathrm{T}} \cdot \bar{\boldsymbol{\varepsilon}} + \mathbf{B}_\phi^{\mathrm{T}} \cdot \boldsymbol{\kappa} \cdot \bar{\mathbf{E}}\right) \mathrm{d}V \\
&\mathbf{f}_u^s = \int_S \left(\mathbf{B}_u^{\mathrm{T}} \cdot \mathbf{e}^s \cdot \bar{\mathbf{E}} - \mathbf{B}_u^{\mathrm{T}} \cdot \mathbf{C}^s \cdot \bar{\boldsymbol{\varepsilon}}\right) \mathrm{d}S, \quad \mathbf{f}_\phi^s = -\int_S \left(\mathbf{B}_\phi^{\mathrm{T}} \cdot \mathbf{e}^{\mathrm{Ts}} \cdot \bar{\boldsymbol{\varepsilon}} + \mathbf{B}_\phi^{\mathrm{T}} \cdot \boldsymbol{\kappa}^s \cdot \bar{\mathbf{E}}\right) \mathrm{d}S
\end{aligned} \quad (44)$$

The local stiffness matrices are assembled into a global system of equations by enforcing the continuities of fluctuating displacements and electric potentials at common nodes of adjacent elements, as well as the periodic conditions at the mirrored faces of a repeating unit cell. The final form of the system of equations for the determination of the fluctuating nodal displacements and electric potentials can be expressed in the following symbolic form:

$$\begin{bmatrix} \mathbb{K}_{uu} & \mathbb{K}_{u\phi} \\ \mathbb{K}_{u\phi}^{\mathrm{T}} & \mathbb{K}_{\phi\phi} \end{bmatrix} \begin{bmatrix} \mathbb{U}' \\ \boldsymbol{\Phi}' \end{bmatrix} = \begin{bmatrix} \mathbb{F}_{u} \\ \mathbb{F}_{\phi} \end{bmatrix} \tag{45}$$

The homogenized generalized stiffness matrix of the unit cell is obtained by sequentially applying one unit strain or electric field to solve the Eq. (45) iteratively for the fluctuating nodal displacements $\mathbb{U}'$ and electrical potentials $\boldsymbol{\Phi}'$, hence the stress and electric displacement fields are obtained. Subsequently, the full set of macroscopic stress and electric displacements for the unit cell are determined through the volume-averaging of their corresponding local fields over the entire volume V and the interface S according to Eq. (9).

5. Numerical Results

The main purpose of this section is to test the accuracy of the developed CCA vis-à-vis the multiphysics FEM model with surface piezoelectricity, the latter of which is currently the computational standard in the simulation community. In this section, numerical results are generated extensively for the first time to demonstrate the effect of surface piezoelectricity on the size-dependent response of piezoelectric nanoporous materials. In the following simulations, the PZT-7A piezoelectric bulk material, as shown in Table 1, has been considered, whose properties were found in (Chen et al., 2018a; Tu and Chen, 2021). The surface parameters are typically identified using atomistic simulations of atomic lattices of finite thickness by progressively decreasing the number of through-thickness atomic planes and extrapolating in the limit to zero (Dai et al., 2011; Miller and Shenoy, 2000; Shenoy, 2005). For instance, most publications (Chen et al., 2018b; Duan et al., 2006) in the literature used the surface parameters, obtained from molecular dynamics simulations for two different crystallographic directions (Miller and Shenoy, 2000). It should be noted that for certain crystallographic orientations of single-crystal metals, the molecular dynamics simulation may produce negative surface moduli, yielding pointwise negative

strain energy density. Thermodynamically there is no restriction about the positiveness of the surface properties (contrarily to a bulk material, whose stiffness tensor needs to be positive definite). However, one needs to verify that the chosen surface parameters do not lead to unstable overall response (Javili et al., 2013; Javili et al., 2012; Wang et al., 2021).

Due to the lack of a complete set of surface parameters for the piezoelectric materials in the open literature, the surface parameters are considered as known quantities. In the continuum mechanics-based simulation of elastic nanostructured materials with the Gurtin-Murdoch interface, the surface parameters obtained by the MD simulation may produce either stiffening or softening behavior of such materials with decreasing nano-pore size depending on whether the surface energies are positive or negative (Chen et al., 2018b). Therefore, in this manuscript, two types of surfaces, labeled as surface A and surface B are utilized unless otherwise stated, which produce negative and positive surface energies, respectively, as shown in Table 2. While a justification of the applicability of the surface parameters with negative surface energy density remains an open question due to the lack of reliable experimental methods, they serve as good candidates for critically assessing the predictive capability of the continuum mechanics-based computational approaches with the extended Gurtin-Murdoch interfaces. The validity of the developed approaches with physically realistic surface parameters for simulating actual piezoelectric nanoporous materials is out of the scope of the present manuscript and will be reported elsewhere in our future publications.

Table 1 Material parameters for the bulk PZT-7A ceramics

$k(\mathrm{GPa})$	$l(\mathrm{GPa})$	$n(\mathrm{GPa})$	$p(\mathrm{GPa})$	$m(\mathrm{GPa})$
112.1	74.24	131	25.30	35.9
$e_{31}\left(\mathrm{Cm}^{-2}\right)$	$e_{33}\left(\mathrm{Cm}^{-2}\right)$	$e_{15}\left(\mathrm{Cm}^{-2}\right)$	$\kappa_{11}\left(\mathrm{nCV}^{-1}\mathrm{m}^{-1}\right)$	$\kappa_{33}\left(\mathrm{nCV}^{-1}\mathrm{m}^{-1}\right)$
-2.324	10.9900	9.31	3.984	2.081

Table 2 Material parameters for the energetic surfaces

Type	$c_{11}^s\left(\mathrm{Nm^{-1}}\right)$	$c_{13}^s\left(\mathrm{Nm^{-1}}\right)$	$c_{33}^s\left(\mathrm{Nm^{-1}}\right)$	$c_{44}^s\left(\mathrm{Nm^{-1}}\right)$	
Surface A	-14.8	-7.424	-13.1	-2.53	
Surface B	29.6	14.84	26.2	5.06	
Type	$e_{31}^s\left(\mathrm{nCm^{-1}}\right)$	$e_{33}^s\left(\mathrm{nCm^{-1}}\right)$	$e_{15}^s\left(\mathrm{nCm^{-1}}\right)$	$\kappa_{11}^s\left(10^{-18}\mathrm{Cm^{-1}}\right)$	$\kappa_{33}^s\left(10^{-18}\mathrm{Cm^{-1}}\right)$
Surface A	0.2324	-1.099	-0.931	-0.3984	-0.2081
Surface B	-0.4648	2.198	1.862	0.7968	0.4162

5.1 Homogenized Properties

In the classical micromechanics methodologies, the composite medium is considered to be statistically homogeneous microstructures in nature which contain the same phase volume fractions and statistical distributions as the material-at-large. In this case, the overall response of unidirectional porous composite is transversely isotropic, characterized by five elastic constants, three piezoelectric constants and two dielectric constants. In the finite-element simulations, if the porosities are randomly distributed or placed periodically in a hexagonal array, the homogenized properties are also transversely isotropic as the classical micromechanics methods. However, finite-element simulations of randomly distributed porosities require statistical analysis of unit cells containing a sufficient number of pore phases such that the statistical distributions of inclusions and their volume fractions are captured. Therefore, the hexagonal repeating unit cell depicted in Figure 5 is adopted for comparison with the CCA/GSCM model, both of which yield the transversely isotropic effective behavior. It is also worth mentioning that Hashin and Rosen (1964) developed the composite cylinder assemblage theory by assuming that "all fibers are surrounded by the largest possible nonoverlapping equal circular cylindrical surfaces" and using hexagonal array as the base for their random array.

The unit cell was discretized into 96×24 four-noded Lagrange elements in the circumferential and radial directions, respectively, which contain 2351 nodes in total with four

degrees (three displacement components and one electric potential) at each node. Gaussian quadrature rule with 5×5 points was utilized to evaluate numerically the local stiffness matrix at each element. The periodicity boundary conditions of fluctuating displacements and electric potential are directly enforced during the assembly of the local stiffness matrices by assigning the same number to the nodes in the mirrored faces when the meshes are generated.

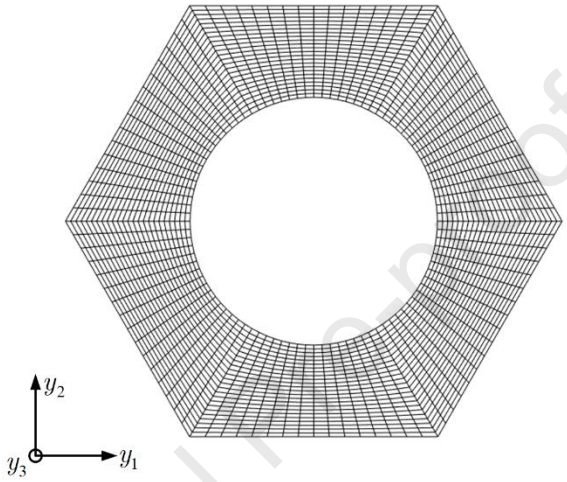

Figure 5 Finite-element mesh discretization of the hexagonal periodic porous array with 30% pore volume fraction for comparison with CCA model

Figures 6-8 show the comparison of the homogenized Hill's moduli, piezoelectric constants, and dielectric constants, normalized by their corresponding values without surface piezoelectricity effect, predicted by the multiphysics FEM and CCA model with incorporated piezoelectricity, as a function of nanopore radii in the range of $0.5nm \le a \le 20nm$ in an increment of $\Delta a = 0.5nm$. The surface piezoelectricity effects are notable for both type A and type B surfaces in this nano-parameter range. The pore volume fraction has been kept as 30%.

As anticipated, while small differences are observed for the effective transverse shear modulus, the CCA predictions correlate remarkably well with the finite-element solutions for all the axisymmetric moduli, axial shear modulus, piezoelectric constants, and dielectric constants at this porosity volume fraction. It should be emphasized that all the predicted properties of these two

families of composites are similar except for the transverse shear modulus where they show marked differences that are reminiscent of what has been observed in the absence of surface electricity. It is also noted that surface A (corresponding to negative surface energies) yields lower effective properties with decreasing the pore dimension relative to the classical results without surface piezoelectricity. An opposite tendency is observed for surface B (corresponding to positive surface energies). For both surfaces, the effect of surface piezoelectricity decreases quickly with the increasing pore radius and almost converges to the results without surface piezoelectricity at $a = 20nm$.

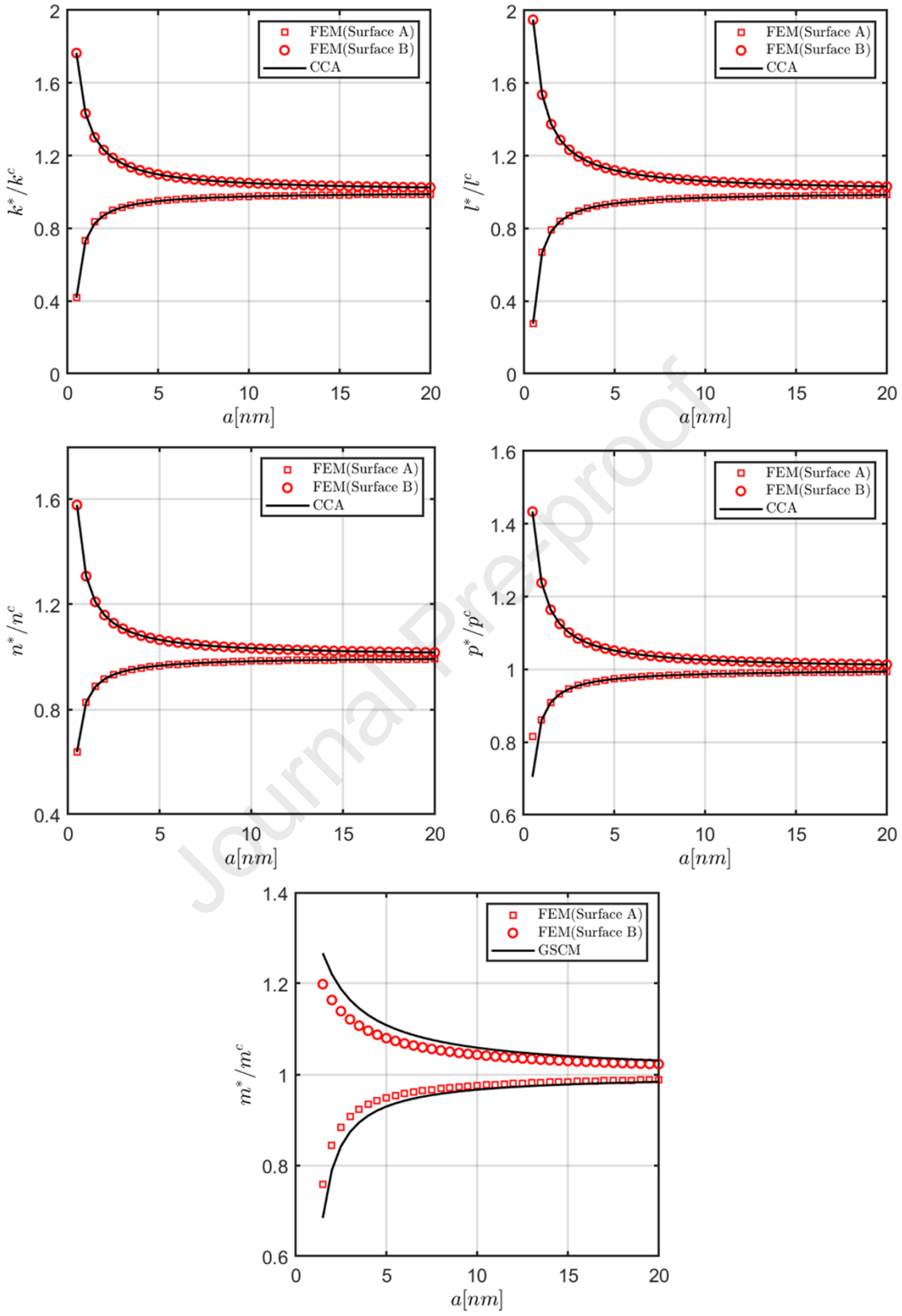

Figure 6 Normalized effective Hill's moduli of a transversely isotropic porous PZT-7A with 0.30 porosity volume fraction as a function of pore radius. Comparison of the multiphysics FEM vis-à-vis CCA/GSCM models

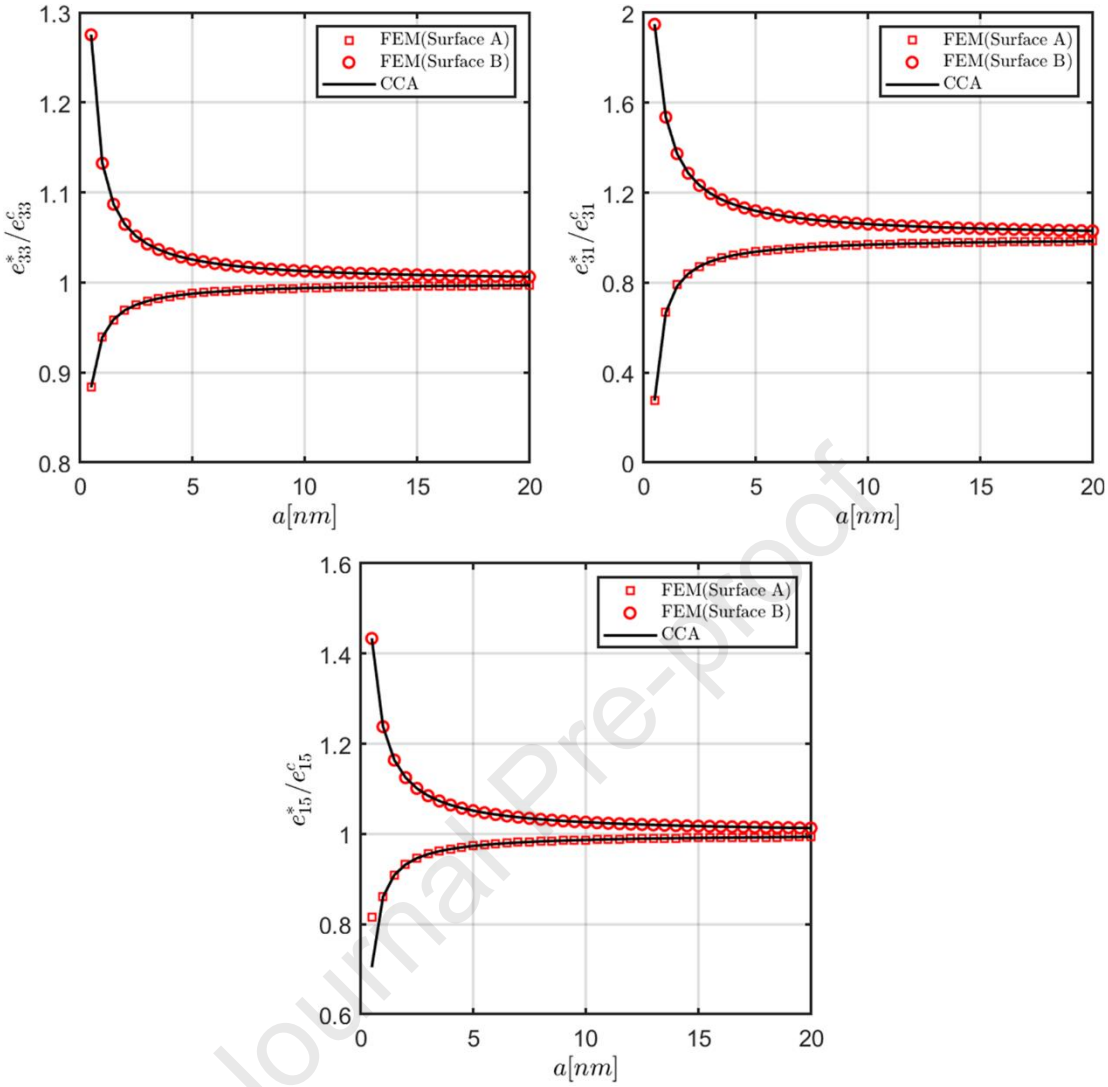

Figure 7 Normalized effective piezoelectric constants of a transversely isotropic porous PZT-7A with 0.30 porosity volume fraction as a function of pore radius. Comparison of the multiphysics FEM vis-à-vis CCA model

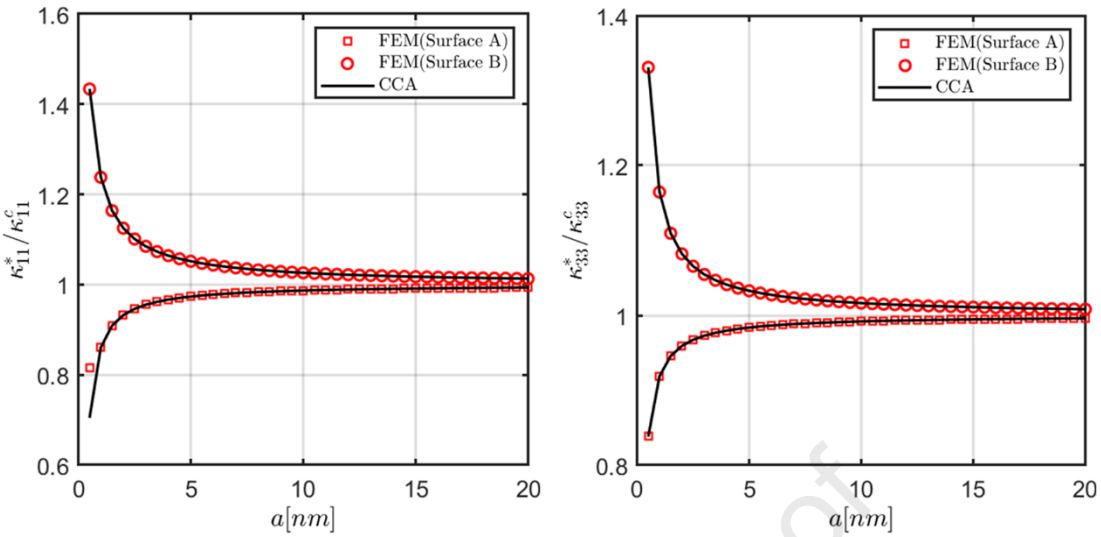

Figure 8 Normalized effective dielectric constants of a transversely isotropic porous PZT-7A with 0.30 porosity volume fraction as a function of pore radius. Comparison of the multiphysics FEM vis-à-vis CCA model

In the second case of the example, the nanopore radii have been kept as $5nm$ and $20\,nm$. Numerical results are generated as a function of pore volume fractions v_f in the range of $[0, 0.5]$ in 0.05 increment for both surfaces A and B, predicted by the CCA and multiphysics FEM enhanced with piezoelectricity. As before, the results in Figures 9-11 are normalized by their corresponding values without surface piezoelectricity. Once again, the effective axisymmetric moduli, axial shear modulus, piezoelectric constants, and dielectric constants predicted by the exact and approximate solutions show a good level of accordance at the entire volume fraction range. In contrast, the differences in the predicted transverse shear moduli by the two computational approaches are significant at the intermediate and high volume fraction ranges, with greater differences observed for the smaller pore radius, namely $a = 5nm$. It is also observed that, at the same pore radii, the effect of surface piezoelectricity becomes more remarkable with increasing pore volume fraction for both types of surfaces, as the pore-pore interactions are more important at the higher volume fractions. The CCA and multiphysics FEM theories accurately capture the effect of surface piezoelectricity on homogenized properties of nanoporous (except for

the transverse shear loading case in the case of GSCM) at a large pore radius and volume fraction ranges, providing good evidence of the accuracy of the developed approaches.

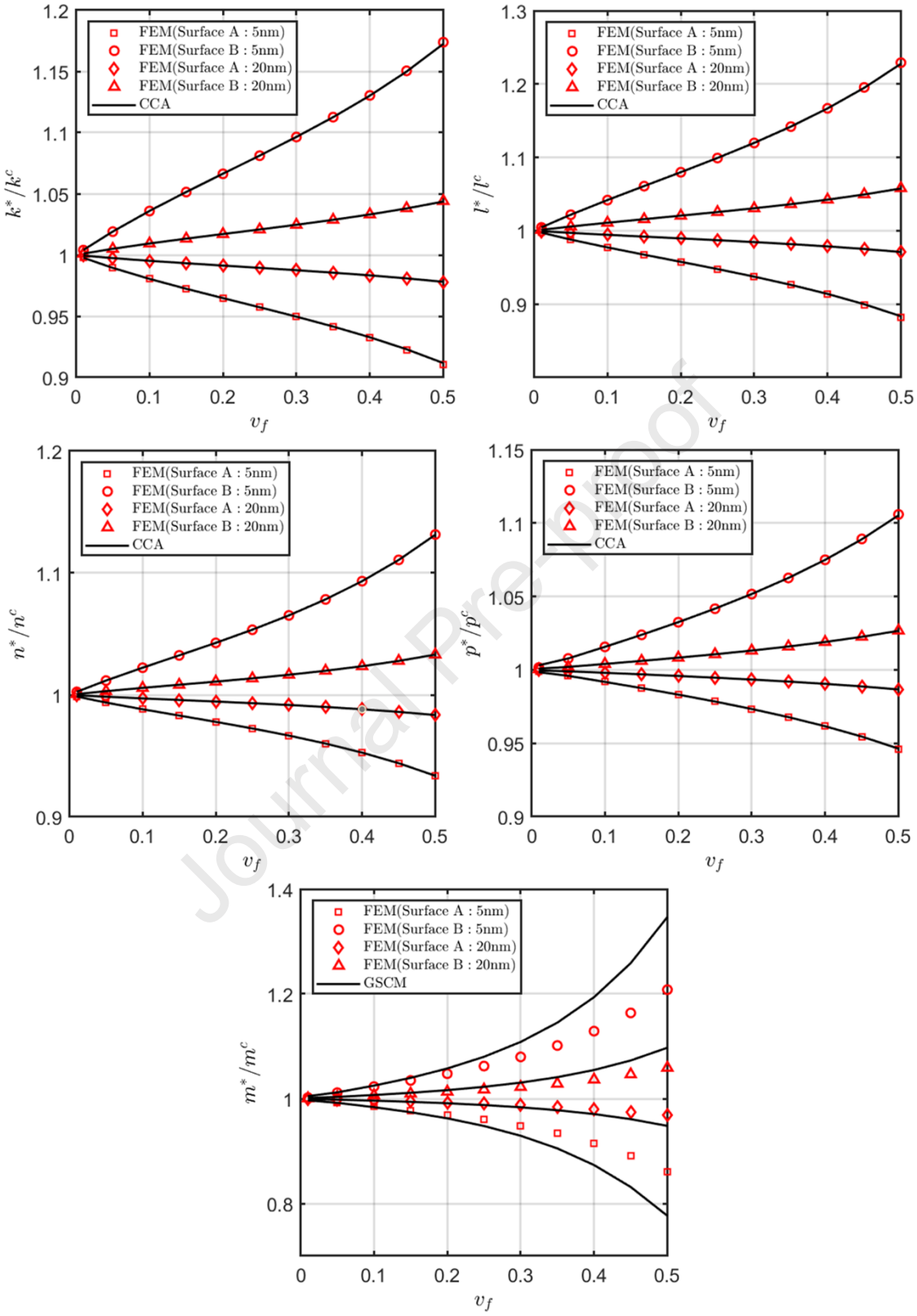

Figure 9 Normalized effective moduli of a transversely isotropic porous PZT-7A as a function of pore volume fraction at the pore radii of $5nm$ and $20nm$. Comparison of the multiphysics FEM vis-à-vis CCA/GSCM model

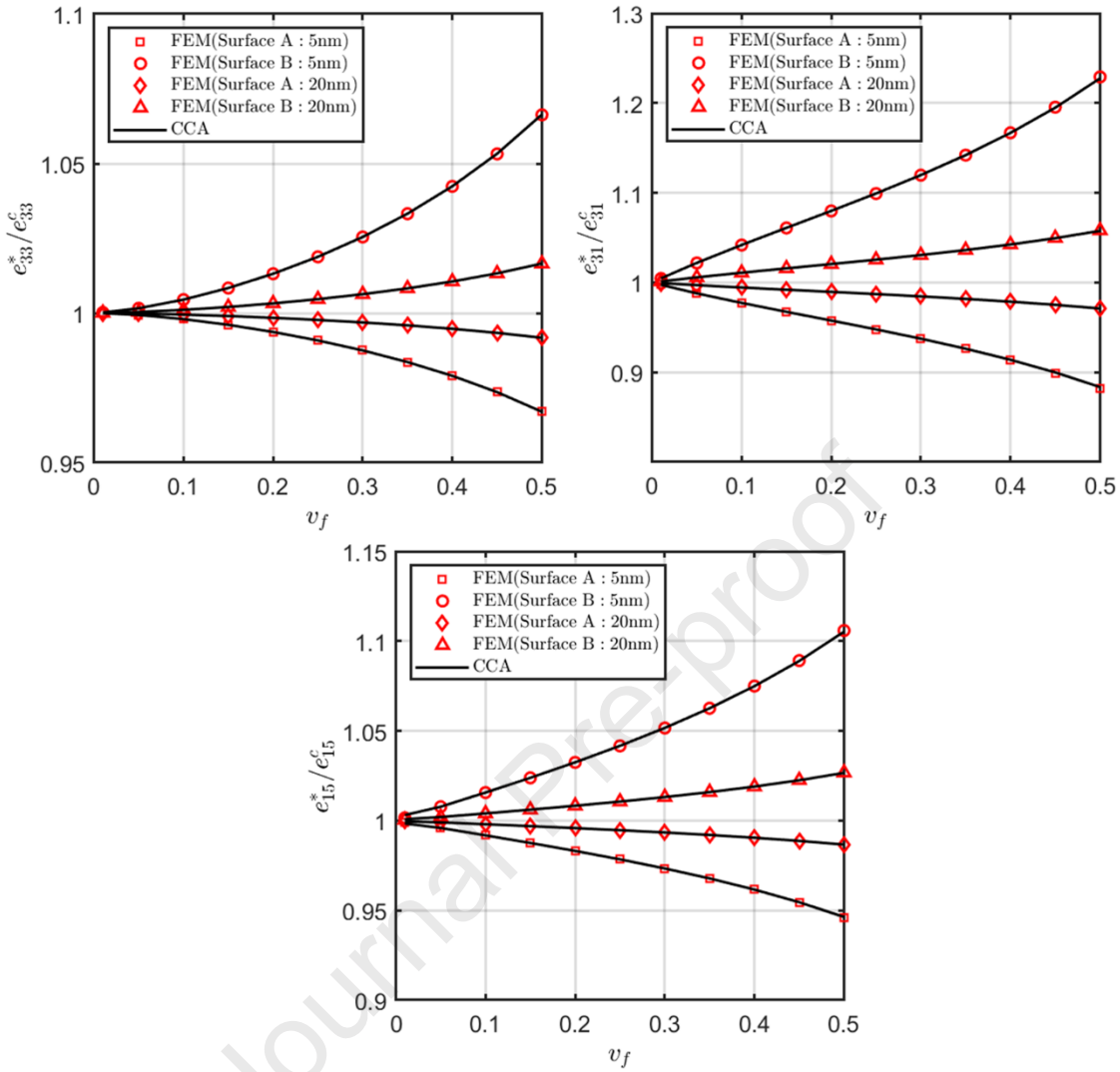

Figure 10 Normalized effective piezoelectric constants of a transversely isotropic porous PZT-7A as a function of pore volume fraction at the two radii of $5nm$ and $20nm$. Comparison of the multiphysics FEM vis-à-vis CCA model

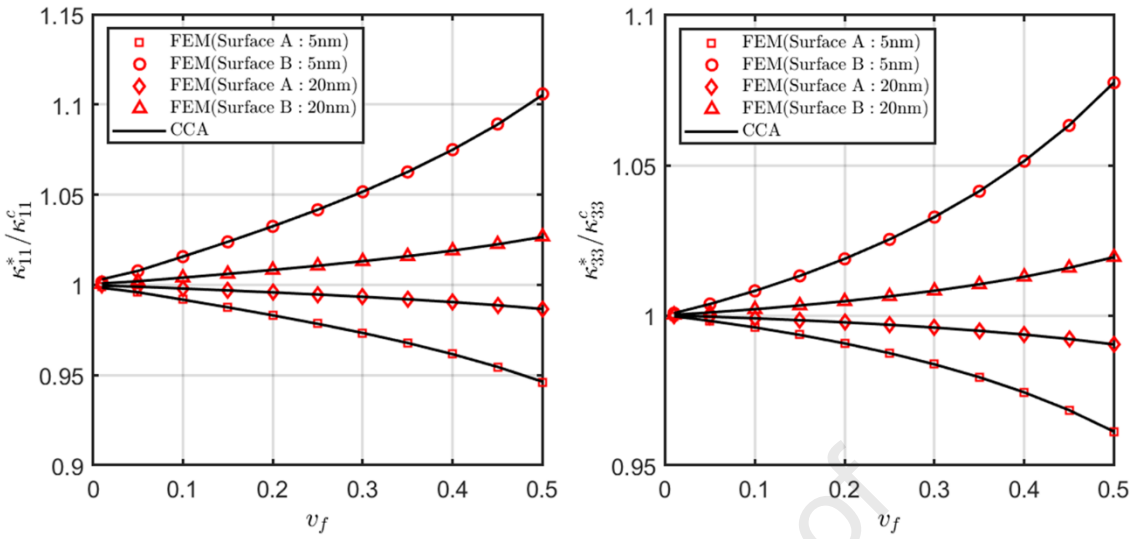

Figure 11 Normalized effective dielectric constants of a transversely isotropic porous PZT-7A as a function of pore volume fraction at the two radii of $5nm$ and $20nm$. Comparison of the multiphysics FEM vis-à-vis CCA model

5.2 Feasibility of the surface parameters

As demonstrated in the previous subsections, due to the negative surface energies, surface A produces a reduction in homogenized moduli relative to the classical results without surface piezoelectricity. The extent of homogenized moduli reduction is strongly influenced by the surface properties, as well as the pore radii and volume fractions. This raises the question of whether the employed surface parameters are physically meaningful since the homogenized moduli of nanoporous composites should retain a positively definite character. Therefore, there exists a limit for the surface constants when they are assumed negative values for any given microstructure (Chatzigeorgiou et al., 2015a). In addition, the surface with negative moduli may produce solution bifurcation. For instance, numerical instabilities associated with the solution of stress fields in nanoporous materials with negative surface energies have been extensively reported in the literature using both analytical and numerical approaches (Chen and Pindera, 2020; Javili et al., 2012; Kochmann and Drugan, 2012; Wang et al., 2021), which prevent the computation of the homogenized moduli for sufficiently small nanopore radii. In contrast, no solution instabilities

have been observed for the surface with positive surface energies over a broad range of pore radii and volume fractions.

In order to generate a reliable set of results, the admissible parameter range needs to be properly established. Figure 12 presents multiphysics finite-element predictions of the normalized homogenized plane strain bulk modulus k^*/k^c, piezoelectric constant e_{31}^*/e_{31}^c and dielectric constant $\kappa_{11}^*/\kappa_{11}^c$ as a function of pore radii at two different volume fractions $v_f = 0.3$ and $v_f = 0.5$. For both type A and B surfaces, two additional sets of surface parameters, which are obtained by multiplying the parameters in Table 2 by factors of $R = 2.5$ and $R = 5$, are used for comparison. As observed, the homogenized moduli predicted by surface A will vanish when the pore radii are sufficiently small. In addition, surface A may produce solution bifurcation in the unit cell boundary value problem due to the significant locally negative surface energies, which is characterized by discontinuities in homogenized property prediction across critical pore radii. Surface B parameter, however, yields smooth variation of the homogenized moduli over the entire pore radius range, without experiencing any numerical instabilities as observed in the surface A case.

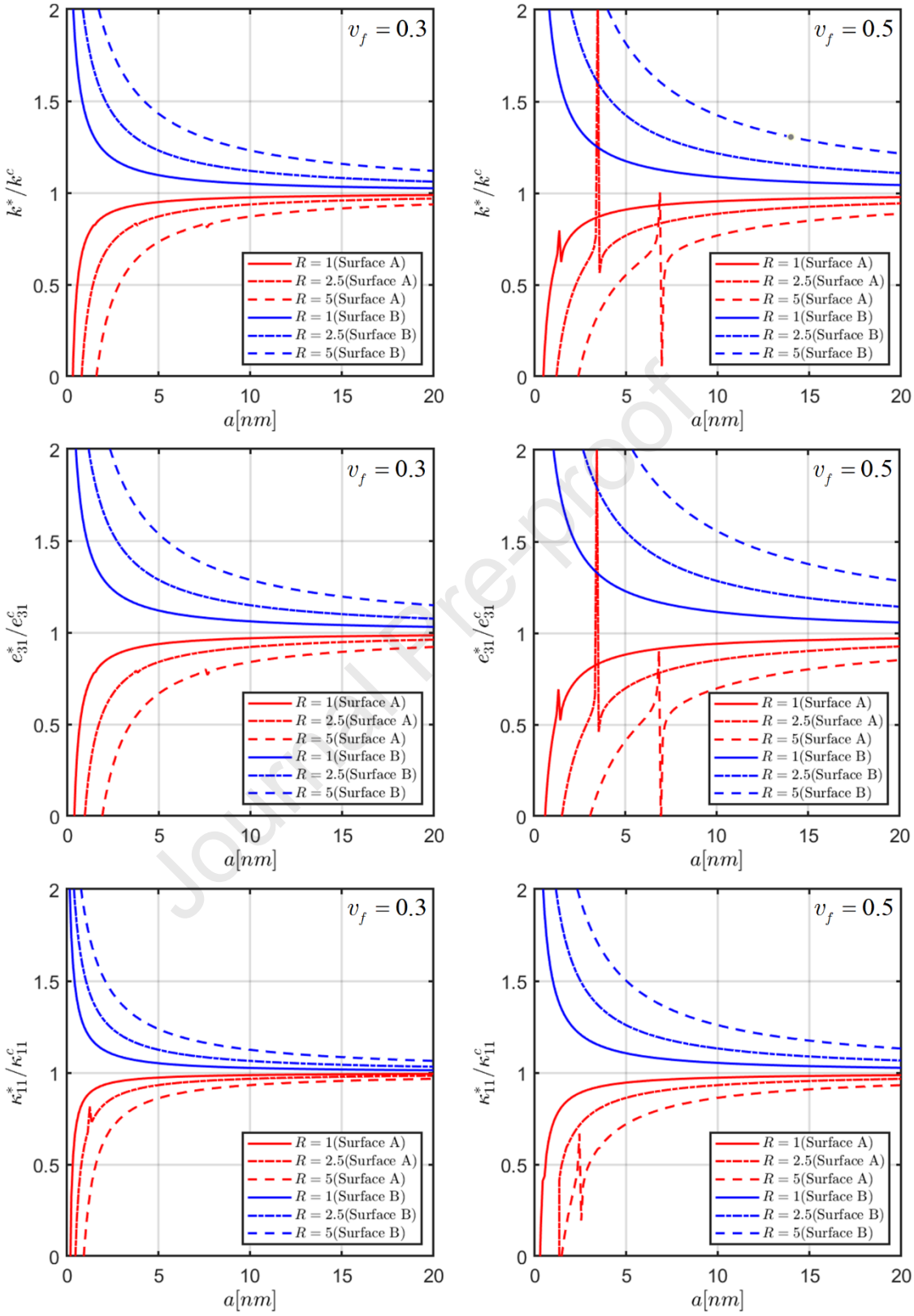

Figure 12 Comparison of the selected homogenized moduli as a function of pore radii at two different volume fractions and three sets of surface properties, illustrating that admissible parameter range needs to be properly established to generate a reliable set of results

6. Conclusion

This manuscript attempts to shed light on surface piezoelectricity effects on the effective size-dependent material properties of nanoporous piezoelectric materials. Kinematically coherent interface that considers the interface traction and electric displacement jump conditions, described by the extended Gurtin--Murdoch model, is adopted. Two novel homogenization techniques based on the extended CCA, GSCM and the multiphysics FEM have been developed to account for the surface effects, which are extensively compared and verified. In the former approach, three systems of equations, under axisymmetric loading, combined axial shear and in-plane electric field loading, as well as transverse shear loading, are derived respectively to obtain the closed-form solutions for the corresponding Hill's moduli, the piezoelectric and dielectric constants. The variation of the surface stress and surface electric displacement is addressed by the generalized Young--Laplace equations, which satisfy the interface stress equilibrium and charge-conservation conditions. In the latter approach, the local and global stiffness matrices for the bulk materials and energetic surfaces are formulated using the minimization of total potential energy. The surface energy effects are incorporated directly through additional surface energies associated with the affected elements that stretch along the pore boundary. The totally different solution techniques, but with remarkable agreements of the homogenized properties between the exact and approximate solutions over a wide parameter space (except for the transverse shear modulus in the case of GSCM), provide strong support for the accuracy of the developed computational tools for simulating the size-dependent multiphysics behaviors of the nanoporous materials. Care must also be taken when the interface with negative surface energies is assumed for nanoporous materials.

Admissible parameter range needs to be properly established in order to generate a reliable set of results.

Acknowledgment

Ali Javili gratefully acknowledges the support provided by the Scientific and Technological Research Council of Turkey (TÜBITAK) Career Development Program, grant number 218M700.

Appendix: Generalized Kirsch Problem with Surface Piezoelectricity

Exact solution for a cylindrical porosity in an infinite plate subjected to far-field loading has been frequently utilized in the literature to validate various homogenization approaches with incorporated surface effects, which is the so-called generalized Kirsch problem with surface piezoelectricity. In the appendix, the analytical solution for electric displacement and antiplane shear stress distributions under the far-field transverse electric displacement loading by $D_x^\infty \neq 0$ and $\sigma_{12}^\infty \neq 0$ is obtained. Using the transformation relation between the Cartesian and cylindrical coordinates, the boundary condition at infinity reads:

$$\begin{aligned} D_r\left(r\to\infty\right) &= D_2^\infty \cos\theta, \quad D_\theta\left(r\to\infty\right) = -D_2^\infty \sin\theta \\ \sigma_{zr}\left(r\to\infty\right) &= \sigma_{12}^\infty \cos\theta, \quad \sigma_{z\theta}\left(r\to\infty\right) = \sigma_{12}^\infty \sin\theta \end{aligned} \tag{A1}$$

The far-field loading in Eq. (A1) can be rewritten in terms of the displacement and electric potential as follows:

$$\lim_{r\to\infty} u_z\left(r,\theta\right) = \varepsilon^o r\cos\theta, \quad \lim_{r\to\infty}\phi\left(r,\theta\right) = -E^o r\cos\theta \tag{A2}$$

The solution of Eq. (A2) that satisfies the stress equilibrium and electrostatic conditions, along with the far-field loading takes the form:

$$\begin{aligned} u_z\left(r,\theta\right) &= \left(\Xi_1 + \Xi_2 r^{-2}\right) r\cos\theta \\ \phi\left(r,\theta\right) &= \left(\Xi_3 + \Xi_4 r^{-2}\right) r\cos\theta \end{aligned} \tag{A3}$$

where Ξ_i ($i=1,..4$) are four unknown coefficients. With the help of the expressions in Eq. (A3), the out-of-plane shear stress σ_{zr} and electric displacement D_r at infinity can be obtained as follows:

$$\begin{aligned}\sigma_{zr}\left(r\to\infty\right)&=\left(p\Xi_1+e_{15}\Xi_3\right)\cos\theta\\ D_r\left(r\to\infty\right)&=\left(e_{15}\Xi_1-\kappa_{11}\Xi_3\right)\cos\theta\end{aligned}\tag{A4}$$

Comparison of Eq. (A4) and Eq. (A1) leads to

$$\begin{bmatrix} p & e_{15}\\ e_{15} & -\kappa_{11}\end{bmatrix}\begin{bmatrix}\Xi_1\\ \Xi_3\end{bmatrix}=\begin{bmatrix}\sigma_{12}^{\infty}\\ D_2^{\infty}\end{bmatrix}\tag{A5}$$

Solution of Eq. (A5) for known σ_{12}^{∞} and D_2^{∞} yields explicit expressions for the coefficients Ξ_1 and Ξ_3. The remaining two equations for the determination of the Ξ_2 and Ξ_4 are given by the Young--Laplace equations at the pore boundary $r=a$:

$$\sigma_{rz}\left(a,\theta\right)=-\frac{1}{a}\frac{\partial\sigma_{\theta z}^{s}}{\partial\theta},\quad D_r\left(a,\theta\right)=-\frac{1}{a}\frac{\partial D_{\theta}^{s}}{\partial\theta}\tag{A6}$$

which produce

$$\begin{bmatrix}-\left(pa^{-2}+c_{44}^{s}a^{-3}\right) & -\left(e_{15}a^{-2}+e_{15}^{s}a^{-3}\right)\\ -\left(e_{15}a^{-2}+e_{15}^{s}a^{-3}\right) & \kappa_{11}a^{-2}+\kappa_{11}^{s}a^{-3}\end{bmatrix}\begin{bmatrix}\Xi_2\\ \Xi_4\end{bmatrix}=-\begin{bmatrix}p-c_{44}^{s}a^{-1} & e_{15}-e_{15}^{s}a^{-1}\\ e_{15}-e_{15}^{s}a^{-1} & -\kappa_{11}+\kappa_{11}^{s}a^{-1}\end{bmatrix}\begin{bmatrix}\Xi_1\\ \Xi_3\end{bmatrix}\tag{A7}$$

Having obtained the solution for the coefficients Ξ_i ($i=1,..4$) from Eqs. (A5) and (A7), the stress and electric displacement field for a given far-field loading D_2^{∞} and σ_{12}^{∞} can be computed by:

$$\begin{aligned}\sigma_{zr}&=p\left(\Xi_1-\Xi_2r^{-2}\right)\cos\theta+e_{15}\left(\Xi_3-\Xi_4r^{-2}\right)\cos\theta\\ \sigma_{z\theta}&=p\left(\Xi_1+\Xi_2r^{-2}\right)\sin\theta-e_{15}\left(\Xi_3+\Xi_4r^{-2}\right)\cos\theta\\ D_r&=e_{15}\left(\Xi_1-\Xi_2r^{-2}\right)\cos\theta-\kappa_{11}\left(\Xi_3-\Xi_4r^{-2}\right)\cos\theta\\ D_{\theta}&=-e_{15}\left(\Xi_1+\Xi_2r^{-2}\right)\sin\theta+\kappa_{11}\left(\Xi_3+\Xi_4r^{-2}\right)\sin\theta\end{aligned}\tag{A8}$$

The finite-element unit cell model for comparison with the generalized Kirsch problem under transverse electric displacement loading contains $v_f = 2\%$ pore volume fraction, as shown in Figure A1. As such, the effect of the periodic boundary condition on the local electric displacement field in the vicinity of the porosity is negligible and the FEM results may be compared directly with the exact solution for one single porosity in an infinite matrix. It is worth mentioning that the Kirsch problem can be also solved using a structural finite-element code with a non-periodic domain with a finite size large enough to approximate the geometry of the central-holed infinite plate. However, due to the piezoelectric coupling effect, under transverse far-field electric loading, non-zero axial shear stress will arise in the analysis domain. As such, a three-dimensional mesh refinement will be required if a structural finite-element code is employed. In contrast, the present homogenized version of the finite-element code employs the generalized plane strain constraint. The two-dimensional unit cell discretization is sufficient to capture the axial shear deformation without resorting to the computationally demanding three-dimensional solution. The unit cell was discretized into 96×48 four-noded Lagrange elements in circumferential and radial directions, respectively which contain 4655 nodes in total. The transverse electric displacement loading by $\bar{D}_x = D_x^{\infty}$ replaces the far-field loading in the exact solution.

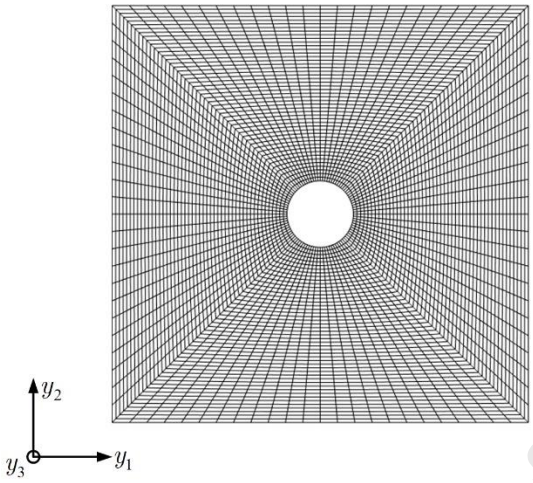

Figure A1 Finite-element mesh discretization for simulating the far-field transverse electric loading

Figures A2-A3 present comparison between the local electric displacement field D_x and D_y distributions predicted by the multiphysics FEM enhanced with surface piezoelectricity and the exact solution for $D_x^{\infty} = 1\ \mathrm{Cm}^{-2}$ for the types A and B surfaces. It is observed a good agreement of the local electric field profiles between the exact and approximate solutions. In the vicinity of the pore boundary, the electric displacement concentrations predicted by the MFEM match very well the exact results, and the distributions themselves are nearly identical. In particular, for both the MFEM and exact solutions, surface A produces a higher concentration of electric displacement at the $\theta = \pm\pi/2$ of the pore boundary, relative to the classical results without surface piezoelectricity (not shown). In contrast, an opposite trend is observed for the surface B case. Additionally, a cursory examination of the local electric displacement distributions reveals a slight difference between the exact solution and MFEM results near the boundary of the square, which is due to the differences in the applied boundary conditions. The MFEM captures these small effects in the applied boundary conditions different from the exact solution, providing additional support for the developed approaches.

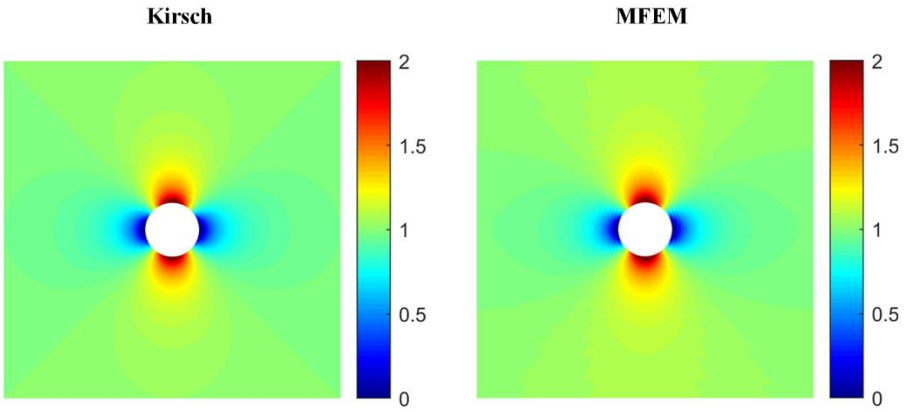

(a) D_x

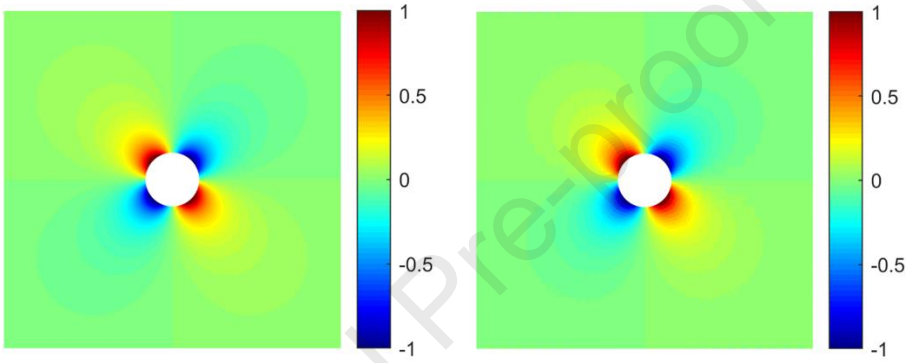

(b) D_y

Figure A2 Comparison of the electric displacement field generated by exact solution and multiphysics FEM under far-field loading by $D_x^{\infty} = 1\ \mathrm{Cm}^{-2}$ at the nanopore radius of $a = 1nm$ for Surface A properties

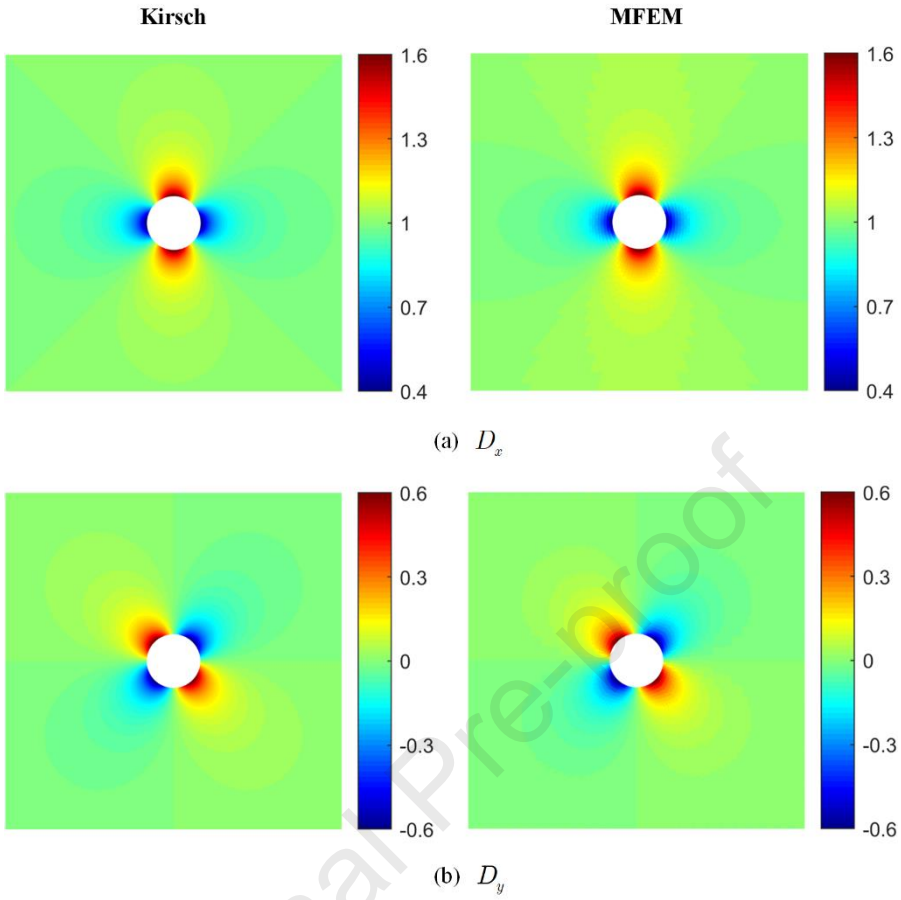

Figure A3 Comparison of the electric displacement field generated by exact solution and multiphysics FEM under far-field loading by $D_x^{\infty} = 1\ \mathrm{Cm}^{-2}$ at the nanopore radius of $a = 1nm$ for Surface B properties

References

Barenblatt, G.I., 1959. The formation of equilibrium cracks during brittle fracture. General ideas and hypotheses. Axially-symmetric cracks. Journal of Applied Mathematics and Mechanics 23, 622-636.

Barenblatt, G.I., 1962. The Mathematical Theory of Equilibrium Cracks in Brittle Fracture, in: Dryden, H.L., von Kármán, T., Kuerti, G., van den Dungen, F.H., Howarth, L. (Eds.), Advances in Applied Mechanics. Elsevier, pp. 55-129.

Bensoussan, A., Lions, J.-L., Papanicolau, G., 1978. Asymptotic analysis for periodic structures. North Holland, Amsterdam.

Benveniste, Y., 2006. A general interface model for a three-dimensional curved thin anisotropic interphase between two anisotropic media. Journal of the Mechanics and Physics of Solids 54, 708-734.

Benveniste, Y., Miloh, T., 2001. Imperfect soft and stiff interfaces in two-dimensional elasticity. Mechanics of Materials 33, 309-323.

Bormann, F., Peerlings, R.H.J., Geers, M.G.D., 2019. On the competition between dislocation transmission and crack nucleation at phase boundaries. European Journal of Mechanics - A/Solids 78, 103842.

Cavalcante, M.A.A., Khatam, H., Pindera, M.-J., 2011. Homogenization of elastic–plastic periodic materials by FVDAM and FEM approaches – An assessment. Composites Part B: Engineering 42, 1713-1730.

Chatzigeorgiou, G., Benaarbia, A., Meraghni, F., 2019a. Piezoelectric-piezomagnetic behaviour of coated long fiber composites accounting for eigenfields. Mechanics of Materials 138, 103157.

Chatzigeorgiou, G., Charalambakis, N., Chemisky, Y., Meraghni, F., 2018. Thermomechanical behavior of dissipative composite materials. Elsevier.

Chatzigeorgiou, G., Javili, A., Meraghni, F., 2019b. Micromechanical method for effective piezoelectric properties and electromechanical fields in multi-coated long fiber composites. International Journal of Solids and Structures 159, 21-39.

Chatzigeorgiou, G., Javili, A., Steinmann, P., 2015a. Interface properties influence the effective dielectric constant of composites. Philosophical Magazine 95, 3402-3412.

Chatzigeorgiou, G., Javili, A., Steinmann, P., 2015b. Multiscale modelling for composites with energetic interfaces at the micro- or nanoscale. Mathematics and Mechanics of Solids 20, 1130-1145.

Chatzigeorgiou, G., Meraghni, F., Charalambakis, N., 2022. Chapter 1 - Tensors, in: Chatzigeorgiou, G., Meraghni, F., Charalambakis, N. (Eds.), Multiscale Modeling Approaches for Composites. Elsevier, pp. 3-27.

Chatzigeorgiou, G., Meraghni, F., Javili, A., 2017. Generalized interfacial energy and size effects in composites. Journal of the Mechanics and Physics of Solids 106, 257-282.

Chebanenko, V.A., Zhilyaev, I.V., Soloviev, A.N., Cherpakov, A.V., Parinov, I.A., 2020. Numerical optimization of the piezoelectric generators. Journal of Advanced Dielectrics 10, 2060016.

Chen, Q., Pindera, M.-J., 2020. Homogenization and localization of elastic-plastic nanoporous materials with Gurtin-Murdoch interfaces: An assessment of computational approaches. International Journal of Plasticity 124, 42-70.

Chen, Q., Sun, Y., Wang, G., Pindera, M.-J., 2019. Finite-volume homogenization and localization of nanoporous materials with cylindrical voids. Part 2: New results. European Journal of Mechanics - A/Solids 73, 331-348.

Chen, Q., Tu, W., Liu, R., Chen, X., 2018a. Parametric multiphysics finite-volume theory for periodic composites with thermo-electro-elastic phases. Journal of Intelligent Material Systems and Structures 29, 530-552.

Chen, Q., Wang, G., 2020. Computationally-efficient homogenization and localization of unidirectional piezoelectric composites with partially cracked interface. Composite Structures 232, 111452.

Chen, Q., Wang, G., Pindera, M.-J., 2018b. Homogenization and localization of nanoporous composites-A critical review and new developments. Composites Part B: Engineering 155, 329-368.

Chen, T., 2008. Exact size-dependent connections between effective moduli of fibrous piezoelectric nanocomposites with interface effects. Acta Mechanica 196, 205-217.

Chen, T., Chiu, M.-S., Weng, C.-N., 2006. Derivation of the generalized Young-Laplace equation of curved interfaces in nanoscaled solids. Journal of Applied Physics 100, 074308.

Christensen, R.M., Lo, K.H., 1979. Solutions for effective shear properties in three phase sphere and cylinder models. Journal of the Mechanics and Physics of Solids 27, 315-330.

Craighead, H.G., 2000. Nanoelectromechanical Systems. Science 290, 1532-1535.

Dai, M., Yang, H.-B., Schiavone, P., 2019. Stress concentration around an elliptical hole with surface tension based on the original Gurtin–Murdoch model. Mechanics of Materials 135, 144-148.

Dai, S., Gharbi, M., Sharma, P., Park, H.S., 2011. Surface piezoelectricity: Size effects in nanostructures and the emergence of piezoelectricity in non-piezoelectric materials. Journal of Applied Physics 110, 104305.

Davydov, D., Javili, A., Steinmann, P., 2013. On molecular statics and surface-enhanced continuum modeling of nano-structures. Computational Materials Science 69, 510-519.

Duan, H.L., Karihaloo, B.L., 2007. Thermo-elastic properties of heterogeneous materials with imperfect interfaces: Generalized Levin's formula and Hill's connections. Journal of the Mechanics and Physics of Solids 55, 1036-1052.

Duan, H.L., Wang, J., Karihaloo, B.L., Huang, Z.P., 2006. Nanoporous materials can be made stiffer than non-porous counterparts by surface modification. Acta Materialia 54, 2983-2990.

Dugdale, D.S., 1960. Yielding of steel sheets containing slits. Journal of the Mechanics and Physics of Solids 8, 100-104.

Elices, M., Guinea, G.V., Gómez, J., Planas, J., 2002. The cohesive zone model: advantages, limitations and challenges. Engineering Fracture Mechanics 69, 137-163.

Fan, S., Bi, S., Li, Q., Guo, Q., Liu, J., Ouyang, Z., Jiang, C., Song, J., 2018. Size-dependent Young's modulus in ZnO nanowires with strong surface atomic bonds. Nanotechnology 29, 125702.

Firooz, S., Chatzigeorgiou, G., Meraghni, F., Javili, A., 2019. Homogenization accounting for size effects in particulate composites due to general interfaces. Mechanics of Materials 139, 103204.

Firooz, S., Javili, A., 2019. Understanding the role of general interfaces in the overall behavior of composites and size effects. Computational Materials Science 162, 245-254.

Firooz, S., Steinmann, P., Javili, A., 2021. Homogenization of Composites With Extended General Interfaces: Comprehensive Review and Unified Modeling. Applied Mechanics Reviews 73, 040802.

Ghosh, K., Lopez-Pamies, O., 2022. Elastomers filled with liquid inclusions: Theory, numerical implementation, and some basic results. Journal of the Mechanics and Physics of Solids 166, 104930.

Gu, S.T., Qin, L., 2014. Variational principles and size-dependent bounds for piezoelectric inhomogeneous materials with piezoelectric coherent imperfect interfaces. International Journal of Engineering Science 78, 89-102.

Gurtin, M.E., Murdoch, A.I., 1975. A continuum theory of elastic material surfaces. Archive for rational mechanics and analysis 57, 291-323.

Gurtin, M.E., Murdoch, A.I., 1978. Surface stress in solids. International Journal of Solids and Structures 14, 431-440.

Hashin, Z., 2002. Thin interphase/imperfect interface in elasticity with application to coated fiber composites. Journal of the Mechanics and Physics of Solids 50, 2509-2537.

Hashin, Z., Rosen, B.W., 1964. The Elastic Moduli of Fiber-Reinforced Materials. Journal of Applied Mechanics 31, 223-232.

He, Z., Pindera, M.-J., 2021a. Finite volume based asymptotic homogenization theory for periodic materials under anti-plane shear. European Journal of Mechanics - A/Solids 85, 104122.

He, Z., Pindera, M.-J., 2021b. Locally exact asymptotic homogenization of viscoelastic composites under anti-plane shear loading. Mechanics of Materials 155, 103752.

Hill, R., 1964. Theory of mechanical properties of fiber-strengthened materials: I. elastic behavior. Journal of the Mechanics and Physics of Solids 12, 199-212.

Hoang, M.-T., Yvonnet, J., Mitrushchenkov, A., Chambaud, G., 2013. First-principles based multiscale model of piezoelectric nanowires with surface effects. Journal of Applied Physics 113, 014309.

Javili, A., McBride, A., Steinmann, P., 2013. Thermomechanics of Solids With Lower-Dimensional Energetics: On the Importance of Surface, Interface, and Curve Structures at the Nanoscale. A Unifying Review. Applied Mechanics Reviews 65, 010802.

Javili, A., McBride, A., Steinmann, P., Reddy, B.D., 2012. Relationships between the admissible range of surface material parameters and stability of linearly elastic bodies. Philosophical Magazine 92, 3540-3563.

Javili, A., Steinmann, P., Mosler, J., 2017. Micro-to-macro transition accounting for general imperfect interfaces. Computer Methods in Applied Mechanics and Engineering 317, 274-317.

Jelinska, N., Kalnins, M., Kovalovs, A., Chate, A., 2015. Design of the Elastic Modulus of Nanoparticles-Containing PVA/PVAc Films by the Response Surface Method. Mechanics of Composite Materials 51, 669-676.

Jiang, J., Zhao, J., Pang, S., Meraghni, F., Siadat, A., Chen, Q., 2022. Physics-informed deep neural network enabled discovery of size-dependent deformation mechanisms in nanostructures. International Journal of Solids and Structures 236-237, 111320.

Kochmann, D.M., Drugan, W.J., 2012. Analytical stability conditions for elastic composite materials with a non-positive-definite phase. Proceedings of the Royal Society A: Mathematical, Physical and Engineering Sciences 468, 2230-2254.

Lefèvre, V., Lopez-Pamies, O., 2015. The Overall Elastic Dielectric Properties of Fiber-Strengthened/Weakened Elastomers. Journal of Applied Mechanics 82, 111009.

Lefèvre, V., Lopez-Pamies, O., 2017. Homogenization of Elastic Dielectric Composites with Rapidly Oscillating Passive and Active Source Terms. SIAM Journal on Applied Mathematics 77, 1962-1988.

Malgras, V., Ataee-Esfahani, H., Wang, H., Jiang, B., Li, C., Wu, K.C.-W., Kim, J.H., Yamauchi, Y., 2016. Nanoarchitectures for Mesoporous Metals. Advanced Materials 28, 993-1010.

Miller, R.E., Shenoy, V.B., 2000. Size-dependent elastic properties of nanosized structural elements. Nanotechnology 11, 139-147.

Milton, G.W., 1985. The coherent potential approximation is a realizable effective medium scheme. Communications in Mathematical Physics 99, 463-500.

Mogilevskaya, S.G., Crouch, S.L., Stolarski, H.K., Benusiglio, A., 2010. Equivalent inhomogeneity method for evaluating the effective elastic properties of unidirectional multi-phase composites with surface/interface effects. International Journal of Solids and Structures 47, 407-418.

Nasedkin, A.V., 2021. Modelling of Piezocomposites with Mechanical Interface Effects, in: Marmo, F., Sessa, S., Barchiesi, E., Spagnuolo, M. (Eds.), Mathematical Applications in Continuum and Structural Mechanics. Springer International Publishing, Cham, pp. 13-31.

Needleman, A., 1987. A continuum model for void nucleation by inclusion debonding. Journal of Applied Mechanics 54, 525-531.

Nguyen, T.D., Mao, S., Yeh, Y.-W., Purohit, P.K., McAlpine, M.C., 2013. Nanoscale Flexoelectricity. Advanced Materials 25, 946-974.

On, D.V., Vuong, L.D., Chuong, T.V., Quang, D.A., Tuyen, H.V., Tung, V.T., 2021. Influence of sintering behavior on the microstructure and electrical properties of BaTiO3 lead-free ceramics from hydrothermal synthesized precursor nanoparticles. Journal of Advanced Dielectrics 11, 2150014.

Saeb, S., Steinmann, P., Javili, A., 2016. Aspects of Computational Homogenization at Finite Deformations: A Unifying Review From Reuss' to Voigt's Bound. Applied Mechanics Reviews 68, 050801.

Shenoy, V.B., 2005. Atomistic calculations of elastic properties of metallic fcc crystal surfaces. Physical Review B 71, 094104.

Thabet, A., Fouad, M., 2021. Assessment of dielectric strength and partial discharges patterns in nanocomposites insulation of single-core power cables. Journal of Advanced Dielectrics 11, 2150022.

Tu, W., Chen, Q., 2020a. Evolution of interfacial debonding of a unidirectional graphite/polyimide composite under off-axis loading. Engineering Fracture Mechanics, 230, 106947.

Tu, W., Chen, Q., 2020b. Homogenization and localization of unidirectional fiber-reinforced composites with evolving damage by FVDAM and FEM approaches: A critical assessment. Engineering Fracture Mechanics 239, 107280.

Tu, W., Chen, Q., 2021. Electromechanical response of multilayered piezoelectric BaTiO3/PZT-7A composites with wavy architecture. Journal of Intelligent Material Systems and Structures 32, 1966-1986.

Tu, W., Pindera, M.-J., 2014. Cohesive zone-based damage evolution in periodic materials via finite-volume homogenization. Journal of Applied Mechanics 81, 101005.

van den Bosch, M.J., Schreurs, P.J.G., Geers, M.G.D., 2007. A cohesive zone model with a large displacement formulation accounting for interfacial fibrilation. European Journal of Mechanics - A/Solids 26, 1-19.

Wang, G., He, Z., Chen, Q., 2021. The surface effects on solid and hollow nanowires under diametral loading. Applied Mathematical Modelling 96, 697-718.

Winter, N., Becton, M., Zhang, L., Wang, X., 2017. Effects of pore design on mechanical properties of nanoporous silicon. Acta Materialia 124, 127-136.

Xiao, J.H., Xu, Y.L., Zhang, F.C., 2011. Size-dependent effective electroelastic moduli of piezoelectric nanocomposites with interface effect. Acta Mechanica 222, 59.

Xu, X.P., Needleman, A., 1994. Numerical simulations of fast crack growth in brittle solids. Journal of the Mechanics and Physics of Solids 42, 1397-1434.

Yang, L., Wang, Y., Guo, Y., Zhang, W., Zhao, Z., 2019. Robust Working Mechanism of Water Droplet-Driven Triboelectric Nanogenerator: Triboelectric Output versus Dynamic Motion of Water Droplet. Advanced Materials Interfaces 6, 1901547.

Yang, L., Wang, Y., Zhao, Z., Guo, Y., Chen, S., Zhang, W., Guo, X., 2020. Particle-Laden Droplet-Driven Triboelectric Nanogenerator for Real-Time Sediment Monitoring Using a Deep Learning Method. ACS Applied Materials & Interfaces 12, 38192-38201.

Yang, S.Y., Jeon, G., Kim, J.K., 2012. A high density array of free standing alumina nanotubes aligned vertically on solid substrates in a large area. Journal of Materials Chemistry 22, 23017-23021.

Yu, J., Wen, Y., Yang, L., Zhao, Z., Guo, Y., Guo, X., 2022. Monitoring on triboelectric nanogenerator and deep learning method. Nano Energy 92, 106698.

Zhang, Y., Hong, J., Liu, B., Fang, D., 2009. Strain effect on ferroelectric behaviors of BaTiO3nanowires: a molecular dynamics study. Nanotechnology 21, 015701.

- Homogenization approaches for piezoelectric composites with energetic interfaces
- Mean field and full field multiphysics analyses accounting for interface effects
- Extended Kirsch problem accounting for surface piezoelectricity
- Excellent agreement between analytical and numerical methods except for transverse shear moduli predictions

AUTHORSHIP STATEMENT Manuscript title:

Homogenization of Size-dependent Multiphysics Behavior of Nanostructured Piezoelectric Composites with Energetic Surfaces

Qiang Chen: Writing - Original Draft, Formal Analysis, Investigation, Validation
George Chatzigeorgiou: Writing - Review & Editing, Conceptualization, Project administration
Fodil Meraghni: Conceptualization, Methodology, Writing - Review & Editing, Formal Analysis
Ali Javili: Conceptualization, Methodology, Writing - Review & Editing

Declaration of interests

☒ The authors declare that they have no known competing financial interests or personal relationships that could have appeared to influence the work reported in this paper.

☐ The authors declare the following financial interests/personal relationships which may be considered as potential competing interests: